

# Broad-band and H $\alpha$ surface photometry of the central regions of nearby active galaxies – I. Observations

Miguel Sánchez-Portal,<sup>1,2★</sup> Ángeles I. Díaz,<sup>1</sup> Roberto Terlevich,<sup>3†</sup> Elena Terlevich,<sup>4★‡</sup>  
Mar Álvarez Álvarez<sup>1</sup> and Itziar Aretxaga<sup>4</sup>

<sup>1</sup>*Dpto. de Física Teórica, C-XI, Universidad Autónoma de Madrid, Cantoblanco, 28049 Madrid, Spain*

<sup>2</sup>*LAEFF/INTA, PO Box 50727, 28080 Madrid, Spain*

<sup>3</sup>*Institute of Astronomy, Madingley Road, Cambridge CB3 0HA*

<sup>4</sup>*Instituto Nacional de Astrofísica, Óptica y Electrónica, Tonantzintla, Puebla, Mexico*

Accepted 1999 September 2. Received 1999 July 12; in original form 1999 April 15

## ABSTRACT

Broad-band *V*, *R* and *I* and narrow-band H $\alpha$  CCD surface photometry of a sample of 24 active and three normal nearby galaxies is presented, in order to study their morphological and structural properties. This first paper presents the observations, data reduction and processing techniques used; the main characteristics of the central regions of the sample galaxies are derived from broad-band and H $\alpha$  images; broad-band surface brightness and colour profiles are presented; based on the inspection of individual images and the examination of the radial variation of ellipticity and polar angle, the morphological class of the sample objects is revised: several objects previously classified as non-barred or unclassified are found to be barred galaxies. A high fraction ( $\sim 71$  per cent) of the objects that present any kind of nuclear activity are barred. This proportion is even higher ( $\sim 87$  per cent) if only Seyfert galaxies are considered. This result can reinforce the clues about the connection between bars and nuclear activity as a fuelling mechanism that can trigger and sustain nuclear activity.

**Key words:** galaxies: active – galaxies: fundamental parameters – galaxies: photometry.

## 1 INTRODUCTION

Many galactic nuclei show signs of more or less violent activity, understood as energy production at a level that cannot be sustained over a large fraction of the expected galaxy life. A substantial fraction of nearby galaxies ( $\approx 40$  per cent; Ho, Filippenko & Sargent 1995) fall into this category, mainly Seyfert, LINER and starburst galaxies. Whether this activity represents a transitory phase in the life of a galaxy or is a fact related to its own structural characteristics still remains an open question.

A number of papers have been written trying to explain the observational aspects of nuclear activity in the light of various theoretical models proposed by different authors (e.g. Rees 1984; Norman & Scoville 1988; Perry 1992; Terlevich 1992). No matter which model is assumed for the nuclear luminosity, an unavoidable fact is the requirement of substantial amounts of gas in the galaxy centre. This gas has to be transported from reservoirs located in the outer parts of the discs, or provided by interactions

with companion galaxies, and in this process it has to get rid of most of its angular momentum. At galactic scales, this can be accomplished by gravitational torques produced in non-axisymmetric potentials in the central regions of these galaxies.

One difficulty in learning about the main processes responsible for the feeding of the nuclear region is that not many papers have been devoted to studying the intrinsic properties of the host galaxies as compared to normal galaxies of similar morphological type. Yee (1983) found the colours of Seyfert galaxies to be comparable to those of normal galaxies of similar type, but their absolute luminosity to be higher. These results have further been confirmed by Kotilainen & Ward (1994) and Hunt et al. (1997).

Heckmann (1980a,b) reported an important result that establishes a basic difference in the Hubble type distribution of galaxies hosting emission-line nuclei, in the sense that galaxies with AGN-like nuclei tend to have Hubble types earlier than Sbc, while those with starburst nuclei tend to have Hubble types later than Sbc. This fact raises the following questions.

(1) Why should this dichotomy in the Hubble type distribution exist at all?

(2) How is it possible that while nuclear star formation is so common in late-type spirals it seems to be almost completely

★ E-mail: msp@vilspa.esa.es (MSP); et@ast.cam.ac.uk (ET)

† Visiting Professor, INAOE, Puebla, Mexico.

‡ Visiting Fellow, IoA, Cambridge.

**Table 1.** Filter characteristics and extinction coefficients.

Filter	$\lambda_c(\text{\AA})$	FWHM( $\text{\AA}$ )	$\tau_{\max}(\text{per cent})$	$k_{\text{atm}}$	$k_{\text{gal}}$
<i>V</i>	5470	938	80	0.1023	3.12
<i>R</i>	6455	1253	87	0.0606	2.56
<i>I</i>	8300	1813	85	0.015	1.74
H $\alpha$ ( $v_r = 0 \text{ km s}^{-1}$ )	6563	53	50	0.0547	2.51
H $\alpha$ ( $v_r = 2000 \text{ km s}^{-1}$ )	6607	53	54	0.0524	2.49
H $\alpha$ ( $v_r = 4000 \text{ km s}^{-1}$ )	6652	49	55	0.0499	2.47
H $\alpha$ ( $v_r = 6000 \text{ km s}^{-1}$ )	6700	53	58	0.0473	2.45
H $\alpha$ ( $v_r = 8000 \text{ km s}^{-1}$ )	6742	47	54	0.0454	2.43
H $\alpha$ ( $v_r = 12000 \text{ km s}^{-1}$ )	6835	50	55	0.0413	2.39

switched off at Sb only two Hubble types away from the peak of their distribution?

(3) As AGN are so common among early-type galaxies, why does their formation seem to be almost completely inhibited at Sc, again only two Hubble types away from the maximum of their distribution?

Arsenault (1989) found that on top of this Hubble type dichotomy there is also a tendency for galaxies with either AGN or starburst nuclei to be associated with bars or rings, with perhaps a slightly higher fraction of bars in starburst nuclei than in AGN.

MacKenty (1990), from a study of the morphologies of a volume- and magnitude-limited sample of Seyfert galaxies, found that  $\approx 70$  per cent of Seyfert galaxies show evidence of the presence of some mechanism for transporting material into their nuclei. The fraction of barred galaxies in his sample is the same as found in normal galaxies, but it is worth noting that some objects classified by MacKenty as spirals (S) may actually possess a bar (e.g., NGC 7469). Regarding the role played by the environment, De Robertis, Hayhoe & Yee (1998) have found that there is no strong evidence that galaxies with AGN are more likely to be associated either with mergers or interactions than normal galaxies of the same type and luminosity.

It seems, therefore, that a detailed high-resolution study of the morphological parameters of galaxies with nuclear activity can contribute significantly towards the understanding of the reasons for certain galaxies to show activity and of the origin of the empirical link between the galaxian morphology and the type of nuclear activity.

With this in mind, we have observed a sample of 24 galaxies which show different degrees of nuclear activity and are sufficiently nearby to provide adequate spatial resolution of their central regions, plus three normal galaxies of comparable morphological type to be used as a reference sample.

This first paper presents the data for the study, while the corresponding analysis will be presented in a forthcoming paper.

## 2 OBSERVATIONS AND DATA REDUCTION

The observations presented here were obtained in two observing runs in 1988 and 1990 using a blue-sensitive GEC CCD at the  $f/15$  Cassegrain focus of the 1.0-m Jacobus Kapteyn Telescope (JKT) of the Isaac Newton Group in La Palma. The CCD size is  $578 \times 385$  pixels, and the pixel size is  $22 \mu\text{m}$ . The scale obtained with this instrumental configuration is  $0.3 \text{ arcsec pixel}^{-1}$ , and the CCD field is  $2.89 \times 1.92 \text{ arcmin}^2$ . Broad-band Kitt Peak *V*, *R* and *I* and narrow-band H $\alpha$  interference filters at the corresponding galaxy rest frame wavelengths were used. Their characteristics are summarized in

Table 1, together with the extinction coefficients used to correct the observations (see below). Columns 1 to 6 give respectively the filter name, central wavelength and FWHM in angstroms, maximum filter transmission, and atmospheric and Galactic extinction coefficients.

The sample consists of 27 galaxies of different morphological type: ellipticals, lenticulars, spirals and irregulars, and with different nuclear activity degree: seven Seyfert type 1, eight Seyfert type 2, six LINER galaxies, three starbursts and three normal galaxies. Nearby objects have been chosen in order to have a good spatial resolution with the instrumental configuration described and the typical seeing conditions ( $0.3 \text{ arcsec pixel}^{-1}$  and a mean seeing of  $1 \text{ arcsec FWHM}$ ). For a typical distance of 18 Mpc, this resolution corresponds to linear dimensions of  $\approx 88 \text{ pc}$ ,<sup>1</sup> approximately the narrow-line region scale size.

The main characteristics of the sample galaxies are summarized in Table 2. Most of the data have been extracted from the NASA/IPAC Extragalactic Database (NED).<sup>2</sup> Morphological types and radial velocities have been taken from de Vaucouleurs et al. (1991) (RC3), except for NGC 4151 for which the radial velocity is given by Pedlar et al. (1993). Nuclear types come from Véron-Cetty & Véron (1985). These types have been checked using the nuclear spectra from Ho et al. (1995) and with the nuclear type information provided by NED.

The journal of observations is presented in Table 3. All observations, except those of H $\alpha$  for NGC 5077, were made under photometric conditions. Every night, photometric and spectrophotometric standards were observed in order to perform the corresponding calibration. Both dome and sky flat-field images were taken, as well as zero-exposure time frames in order to set the bias level. No dark current frames were taken, since, according to Argyle et al. (1988), its mean level is only  $\approx 0.07 \text{ e}^- \text{ pixel}^{-1} \text{ min}^{-1}$ , i.e.,  $2 \text{ e}^-$  in our longest exposures.

The data reduction was carried out using several standard software packages: the Starlink ASPIC and FIGARO sets as implemented in the Royal Greenwich Observatory, the MIDAS package as implemented at the Universidad Autónoma de Madrid, and the IRAF package.

The reduction procedures consisted of subtraction of the bias level of the chip and division by a normalized flat-field. For each image, the bias frame was constructed by adding the mean of the overscan columns to a ‘mean bias noise frame’ obtained from the average of all the bias frames taken during the night.

<sup>1</sup> All distances and linear sizes have been calculated from the radial velocities listed in Table 2, assuming  $H_0 = 55 \text{ km s}^{-1} \text{ Mpc}^{-1}$  and  $q_0 = 0$ .

<sup>2</sup> The NASA/IPAC Extragalactic Database (NED) is operated by the Jet Propulsion Laboratory, California Institute of Technology, under contract with the National Aeronautics and Space Administration.

**Table 2.** Main characteristics of the sample galaxies.

Galaxy	$\alpha$ (1950)			$\delta$ (1950)			Morphological type	Nuclear type	$B_T$	$v_r$ km s <sup>-1</sup>
	h	m	s	°	'	"				
NGC 3227	10	20	46.78	+20	07	06.14	SAB(s) pec	Sy1.5	11.1	1157 ± 3
NGC 3516	11	03	22.84	+72	50	20.22	(R)SB(s)0 <sup>0</sup>	Sy1.5	12.5	2602 ± 7
NGC 3998	11	55	20.93	+55	43	54.58	SA(r)0 <sup>0</sup> ?	Sy1.5	11.61	1040 ± 13
NGC 7469	12	00	44.43	+08	36	16.12	(R')SAB(rs)a	Sy1	13.0	4898 ± 5
NGC 4151	12	08	1.055	+39	41	01.82	(R')SAB(rs)ab	Sy1.5	11.5	997 ± 4
NGC 5077	13	16	53.00	-12	23	43.0	E3-4	Sy1	12.38	2832 ± 45
NGC 6814	19	39	55.79	-10	26	33.35	SAB(rs)bc	Sy1	12.06	1563 ± 4
NGC 513	01	21	37.32	+33	32	21.00	S?	Sy2	13.9	5859 ± 10
NGC 1068	02	40	07.08	-00	13	31.48	(R)SA(rs)b	Sy2	9.61	1136 ± 4
Mrk 620 (NGC 2273)	06	45	37.69	+60	54	12.9	SB(r)a	Sy2	12.55	1840 ± 4
Mrk 622	08	04	21.04	+39	08	58.80	S?	Sy2	14.60	6964 ± 11
NGC 3982	11	53	52.32	+55	24	12.34	SAB(r)b	Sy2	11.78	1109 ± 6
NGC 5347	13	51	04.95	+33	44	11.32	(R')SB(rs)ab	Sy2	13.4	1335 ± 20
NGC 6217	16	35	5.10	+78	18	5.0	(R)SB(rs)bc	Sy2	11.79	1362 ± 4
NGC 7479	23	02	26.37	+12	03	10.6	SB(s)c	Sy2	11.60	2382 ± 2
NGC 1052	02	38	37.35	-08	28	09.02	E4	LINER	11.41	1470 ± 11
NGC 2841	09	18	35.85	+51	11	24.1	SA(r)b	LINER	10.09	638 ± 3
M106 (NGC 4258)	12	16	29.39	+47	34	53.2	SAB(s)bc	LINER	9.10	448 ± 3
M51 (NGC 5194)	13	27	45.98	+47	27	21.5	SA(s)bc pec	LINER	8.96	463 ± 3
NGC 7177	21	58	18.50	+17	29	50.0	SAB(r)b	LINER	12.01	1150 ± 5
NGC 7217	22	05	37.60	+31	06	53.0	(R)SA(r)ab	LINER	11.02	946 ± 4
NGC 2146	06	10	40.10	+78	22	23.0	SB(s)ab pec	starburst	11.38	893 ± 4
NGC 3310	10	35	39.08	53	45	42.6	SAB(r)bc pec	starburst	11.15	980 ± 6
NGC 3353	10	42	15.84	+56	13	26.0	BCD/Irr	starburst	13.25	944 ± 5
NGC 1023	02	37	15.83	+38	50	55.00	SB(rs)0 <sup>-</sup>	normal	10.35	637 ± 4
NGC 6340	17	11	16.90	+72	21	55	SA(s)0/a	normal	11.87	1198 ± 6
NGC 6384	17	29	59.00	+7	05	43.0	SAB(r)bc	normal	11.14	1663 ± 9

Sky subtraction was performed by averaging the mean count values in several boxes in the periphery of the frame, after rejection of those whose standard deviation was greater than 10 per cent. Some objects, like M51, fill the chip entirely, and therefore it was not possible to select sky areas in the galaxy frame. In these cases, the sky level was measured on sky frames taken immediately before and after the object at nearly the same zenith distance.

The final reduction steps involved cosmic rays removal, seeing estimation by a Gaussian fit to the field stars, extinction correction, and calibration with standard stars. Both atmospheric and Galactic extinction correction were applied. The former was calculated using the first-order extinction coefficients provided by La Palma observatory (see Table 1); these values have been checked, and found to be in very good agreement with those derived from our observations of standard stars through a wide range of air masses. Galactic extinction coefficients were computed through the expression  $A_\lambda = k_\lambda E(B - V)$ , using the values of  $E(B - V)$  from Burstein & Heiles (1984) and the absorption constants  $k_\lambda$  interpolated for our filter wavelengths in the Galactic extinction curve from Seaton (1975) (see Table 1). No internal absorption correction was performed [with the exception of NGC 4151, where a value of  $E(B - V) = 0.05$  derived from UV observations from Penston et al. (1981) has been adopted].

The broad-band *VRI* calibration was performed using the photometric standard stars from Landolt (1983). The absolute errors in the photometry are  $\pm 0.01$  mag for *V*,  $\pm 0.04$  mag for *R*, and  $\pm 0.02$  mag for *I*. The narrow-band  $H\alpha$  images were calibrated using spectrophotometric standards from Stone (1977) and Massey et al. (1988). Formal errors in the calibration are between 0.03 and 0.04 mag for the different velocity filters.

The seeing for each observation was measured using star images present in each frame, except in the case of NGC 3227 for which no stars were present and the seeing was estimated from previous frames.

## 3 RESULTS

### 3.1 Broad-band images

Broad-band images of AGN are difficult to interpret due to the contribution of emission lines to the different filters, mainly  $H\beta$   $\lambda 4861 \text{ \AA}$  and  $[O III] \lambda \lambda 4959, 5007 \text{ \AA}$  to *V*, and  $[O I] \lambda \lambda 6300, 6364 \text{ \AA}$ ,  $H\alpha$   $\lambda 6563 \text{ \AA}$ ,  $[N II] \lambda \lambda 6548, 6584 \text{ \AA}$  and  $[S II] \lambda \lambda 6716, 6731 \text{ \AA}$  to *R*. The *I* filter is virtually free from emission-line contamination. Only  $[S III] \lambda 9069 \text{ \AA}$  enters the filter at 1/5 of the peak transmission.<sup>3</sup> Therefore we can consider the *I* band to reflect the true stellar continuum flux. On the other hand, the spatial characteristics of the emitting gas can be seen in the  $H\alpha$  images.

Figs 1–4 show the *I* images of the inner  $15 \times 15$  arcsec<sup>2</sup> (unless specified) for all the objects in our sample. The *x*- and *y*-axes are given in pixels. North is to the top, and east is to the left.

### 3.2 $H\alpha$ images

To produce the  $H\alpha$  emission image, the continuum adjacent to the line has to be removed. When suitable  $H\alpha$  continuum images existed, they were subtracted from the  $H\alpha$  line + continuum frames after careful alignment. This alignment was performed by translation and rotation, using the centroids of field stars and/or galactic nuclei. When possible, at least three objects in each frame have been used for the alignment. The typical accuracy is better than 0.05 pixel. When the two images to be aligned had different seeing, the image with the better seeing was convolved with the appropriate Gaussian function in order to match the one with the poorer seeing.

When no  $H\alpha$  continuum images are available, two different methods for continuum removal have been used, depending on the relative intensity of the lines close to  $H\alpha$ . The first one uses the

<sup>3</sup>  $O I \lambda 8480 \text{ \AA}$  can also be present, but only in luminous Seyfert 1 galaxies.

Table 3. Journal of observations.

Object	Obs. date (UT)	Filter	Exposure time (sec.)	Seeing FWHM ( $''$ )	Scale (pc pixel $^{-1}$ )	(pc $''$ )
NGC 3227	7-May-1988	V	300	1.3 <sup>a</sup>	30.6	102
		R	300			
		I	300			
NGC 3516	10-May-1988	H $\alpha$ (0 km s $^{-1}$ )	1000	2.1	68.8	229
		V	600			
		R	600			
NGC 3998	11-May-1988	I	600	2.2	27.5	92
		H $\alpha$ (2000 km s $^{-1}$ )	1200			
		V	400			
NGC 7469	23-Oct-1990	R	400	1.8	128.3	432
		I	300			
		H $\alpha$ (2000 km s $^{-1}$ )	600			
NGC 4151	6-May-1988	V	500	1.3	26.4	88
		R	300			
		I	300			
NGC 5077 <sup>b</sup>	11-May-1988	H $\alpha$ (4000 km s $^{-1}$ )	800	1.5	74.9	250
		H $\alpha$ (cont.) (0 km s $^{-1}$ )	1000			
		V	300			
NGC 6814	12-May-1988	R	50	0.8	41.3	138
		I	150			
		H $\alpha$ (0 km s $^{-1}$ )	500			
NGC 513	29-Oct-1990	V	500	1.8	154.9	516
		R	500			
		I	500			
NGC 1068	24-Oct-1990	H $\alpha$ (2000 km s $^{-1}$ )	1000	2.0	30.0	100
		V	900			
		R	900			
Mrk 620	27-Oct-1990	I	800	2.0	48.7	162
		H $\alpha$ (2000 km s $^{-1}$ )	900			
		V	300			
Mrk 622	7-May-1988	R	600	1.1	184.2	614
		I	600			
		H $\alpha$ (6000 km s $^{-1}$ )	1800			
NGC 3982	8-May-1988	V	600	1.9	29.3	98
		R	600			
		I	600			
NGC 5347	12-May-1988	H $\alpha$ (0 km s $^{-1}$ )	1200	1.2	61.7	118
		V	900			
		R	600			
NGC 6217	6-May-1988	I	600	1.4	36.0	120
		H $\alpha$ (2000 km s $^{-1}$ )	1000			
		V	300			
NGC 7479	26-Oct-1990	R	300	1.1	63.0	210
		I	300			
		H $\alpha$ (2000 km s $^{-1}$ )	1000			
NGC 1052	24-Oct-1990	V	500	1.1	38.9	130
		R	400			
		I	300			
NGC 2841	6-May-1988	H $\alpha$ (2000 km s $^{-1}$ )	1000	1.3	16.9	56
		V	500			
		R	300			
NGC 1052	24-Oct-1990	H $\alpha$ (cont.) (12000 km s $^{-1}$ )	1000	1.3	38.9	130
		V	500			
		R	500			
NGC 1052	24-Oct-1990	I	500	1.4	38.9	130
		H $\alpha$ (2000 km s $^{-1}$ )	1000			
		V	500			
NGC 1052	24-Oct-1990	H $\alpha$ (cont.) (12000 km s $^{-1}$ )	1200	1.4	38.9	130
		V	500			
		R	300			
NGC 2841	6-May-1988	H $\alpha$ (2000 km s $^{-1}$ )	1000	0.7	16.9	56
		V	300			
		R	300			

**Table 3** – *continued*

Object	Obs. date (UT)	Filter	Exposure time (sec.)	Seeing FWHM ( $''$ )	Scale (pc pixel $^{-1}$ )	Scale (pc $''$ )
M106 (NGC 4258)	10-May-1988	I	200	0.8	11.9	39
		H $\alpha$ (0 km s $^{-1}$ )	600	0.7		
		V	300	1.8		
		R	300	1.6		
M51 (NGC 5194)	7-May-1988	I	400	1.7	12.2	41
		H $\alpha$ (0 km s $^{-1}$ )	800	1.8		
		V	700	0.9		
		R	300	1.1		
NGC 7177	24-Oct-1990	I	300	1.1	30.4	101
		H $\alpha$ (0 km s $^{-1}$ )	1000	0.9		
		V	600	1.2		
		R	600	1.2		
NGC 7217	26-Oct-1990	I	600	1.0	25.0	83
		H $\alpha$ (2000 km s $^{-1}$ )	2000	1.3		
		H $\alpha$ (cont.) (12000 km s $^{-1}$ )	2000	1.4		
		V	500	1.6		
NGC 2146	26-Oct-1990	R	500	1.6	23.6	79
		I	500	1.6		
		H $\alpha$ (2000 km s $^{-1}$ )	1000	1.8		
		H $\alpha$ (cont.) (12000 km s $^{-1}$ )	2000	1.7		
NGC 3310	7-May-1988	V	300	1.7	25.9	86
		R	300	1.7		
		I	300	1.7		
		H $\alpha$ (0 km s $^{-1}$ )	2000	1.8		
NGC 3353	6-May-1988	H $\alpha$ (cont.) (4000 km s $^{-1}$ )	600	1.8	25.0	83
		V	300	0.8		
		R	300	0.9		
		I	300	0.9		
NGC 1023	24-Oct-1990	H $\alpha$ (0 km s $^{-1}$ )	700	0.8	16.8	56
		V	600	1.6		
		R	600	1.4		
		I	1000	1.7		
NGC 6340	10-May-1988	H $\alpha$ (0 km s $^{-1}$ )	1500	1.5	31.7	106
		V	150	1.8		
		R	150	1.8		
		I	150	1.8		
NGC 6384	10-May-1988	H $\alpha$ (0 km s $^{-1}$ )	800	1.5	44.0	147
		H $\alpha$ (cont.) (8000 km s $^{-1}$ )	1000	1.5		
		V	300	1.6		
		R	300	1.5		
	12-May-1988	I	360	1.4	44.0	147
		H $\alpha$ (2000 km s $^{-1}$ )	300	1.6		
		V	400	1.4		
		R	400	1.4		
		I	900	1.9		

<sup>a</sup>Estimated<sup>b</sup>Non-photometric

broad-band  $R$  image as continuum, and derives the line intensity according to the relation (Terlevich et al. 1991)

$$I_l = \frac{I(\text{H}\alpha)k_R - I(R)k_{\text{H}\alpha}}{\tau(\text{H}\alpha)k_R - \tau(R)k_{\text{H}\alpha}}, \quad (1)$$

where  $I(\text{H}\alpha)$  and  $I(R)$  are the observed intensities (in count s $^{-1}$ ) in the  $\text{H}\alpha$  and  $R$  filters respectively,  $\tau(\text{H}\alpha)$  and  $\tau(R)$  are the corresponding filter transmissions at the redshifted  $\text{H}\alpha$  wavelength (Argyle et al. 1988), and  $k_{\text{H}\alpha}$  and  $k_R$  are defined by

$$k_{\text{H}\alpha} = \int_{\Delta\text{H}\alpha} \tau_{\text{H}\alpha}(\lambda) d\lambda, \quad (2)$$

$$k_R = \int_{\Delta R} \tau_R(\lambda) d\lambda. \quad (3)$$

$\Delta\text{H}\alpha$  and  $\Delta R$  are the filter bandwidths.

This method assumes that the lines included in the  $R$  filter and not in the  $\text{H}\alpha$  one are not important. In some cases, notably in the

case of LINERS where [S II] lines are known to be rather prominent, this is not true. We have then developed an alternative method that assumes the existence of a proportionality factor between the  $R$  and  $I$  continua. In order to obtain the proportionality factor, we computed the mean value of the  $R$ - and  $I$ -band intensities in several areas of the galactic bulge, supposedly not affected by emission-line contamination. The ratio  $I(R)_{\text{mean}}/I(I)_{\text{mean}}$  agrees well with the  $R - I$  colour of an old stellar population.

On the other hand, the relationship between the instrumental intensities of the  $\text{H}\alpha$  and  $R$  continua can be computed as

$$\frac{I_c(\text{H}\alpha)}{I_c(R)} \approx \frac{k_{\text{H}\alpha}}{k_R}. \quad (4)$$

This assumes that the continuum in  $R$  is effectively constant. (This value can also be obtained measuring the mean intensity values through the  $\text{H}\alpha$  and  $R$  filters in a region free of emission lines.)

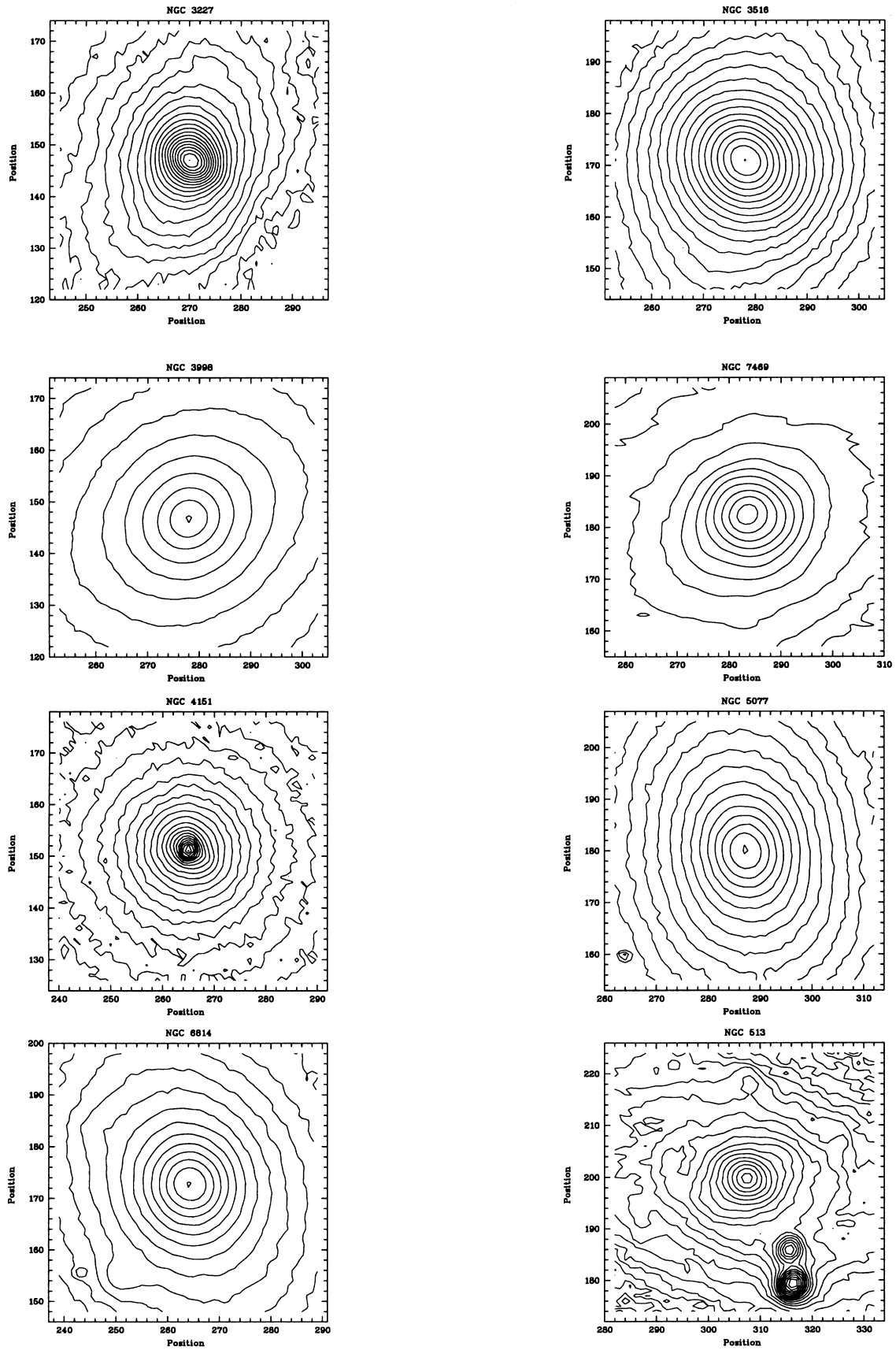


Figure 1. *I*-band isophotal maps of the central regions of the sample galaxies.

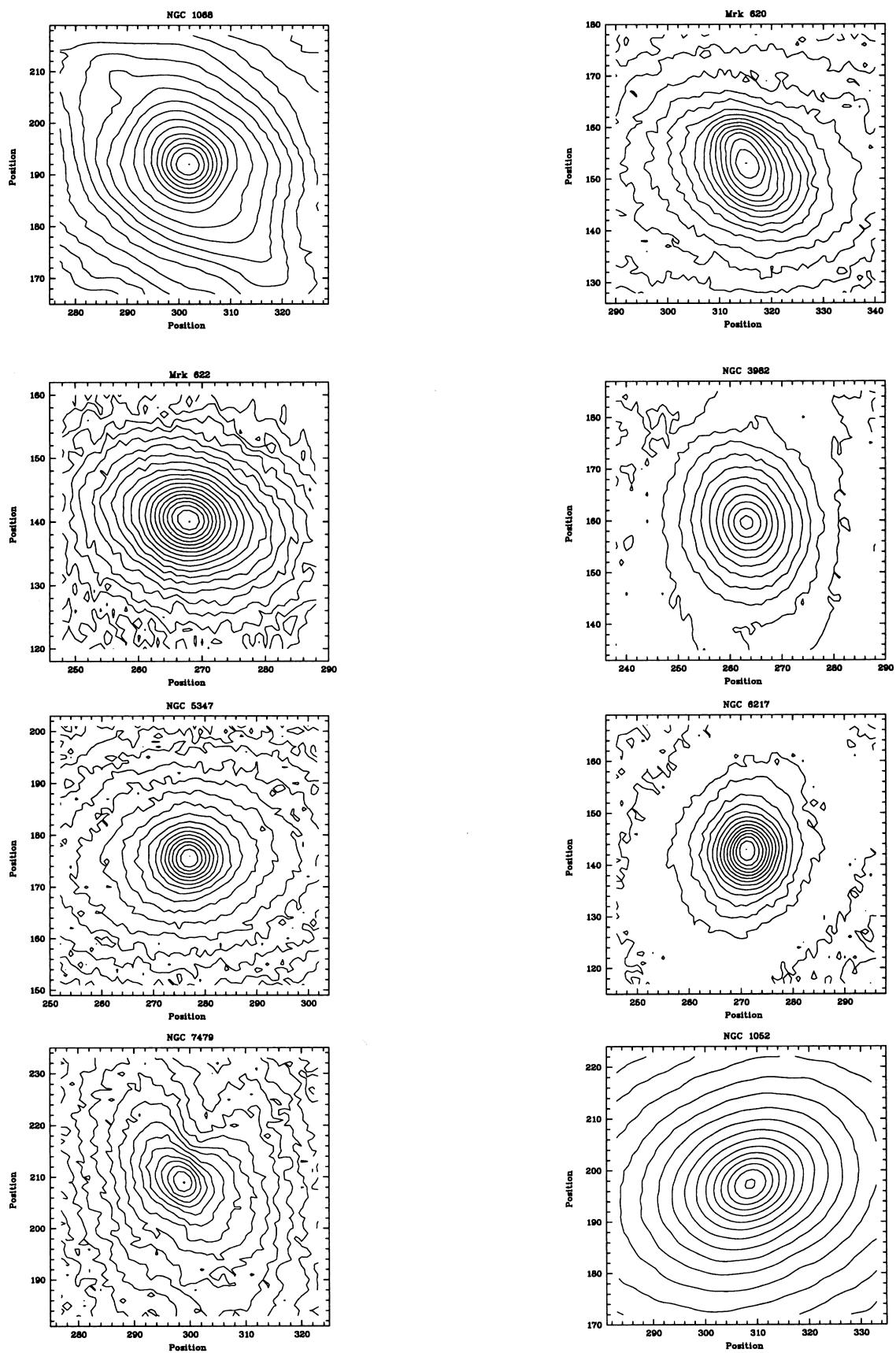


Figure 2. *I*-band isophotal maps of the central regions of the sample galaxies (continued).

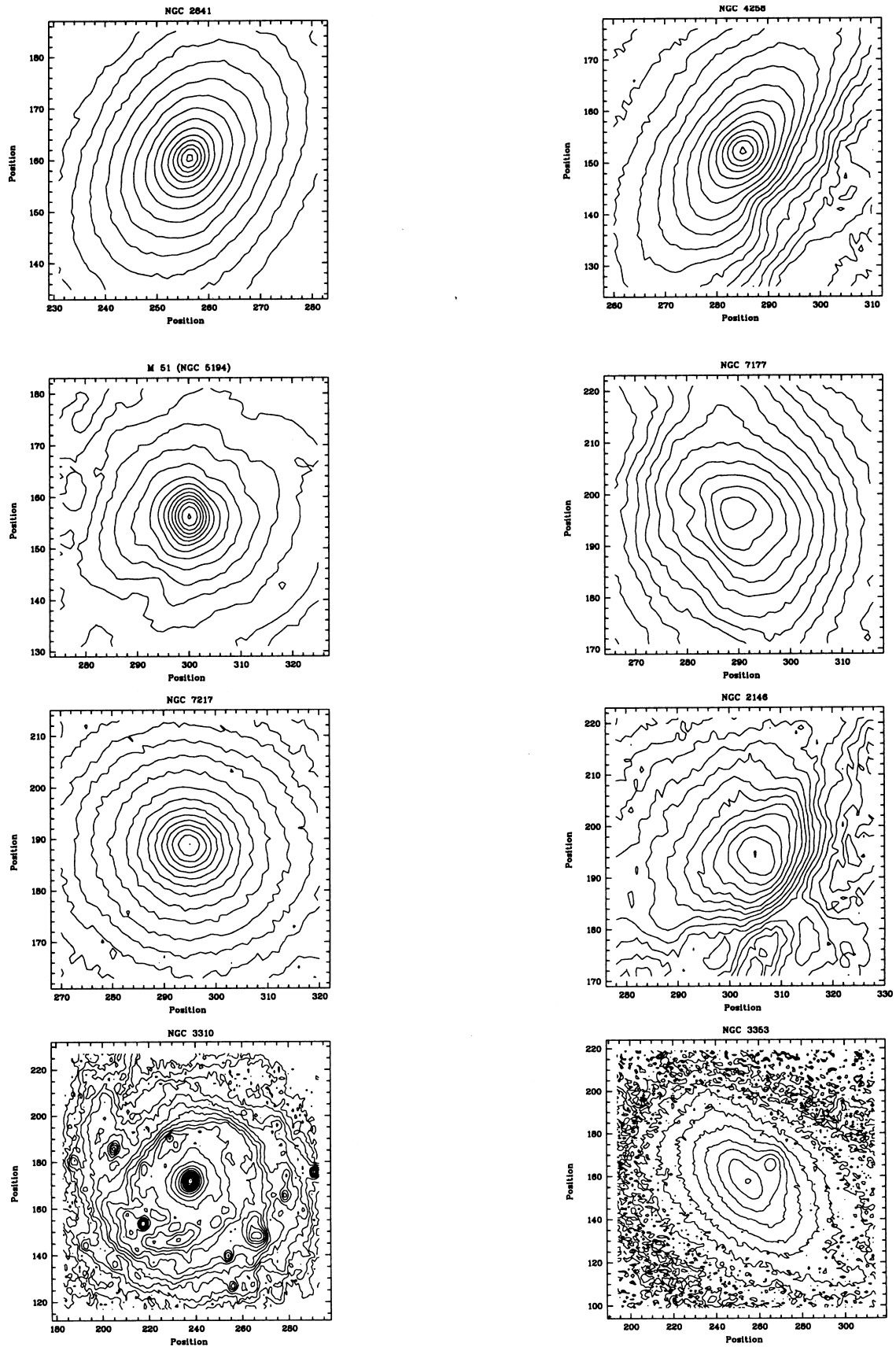
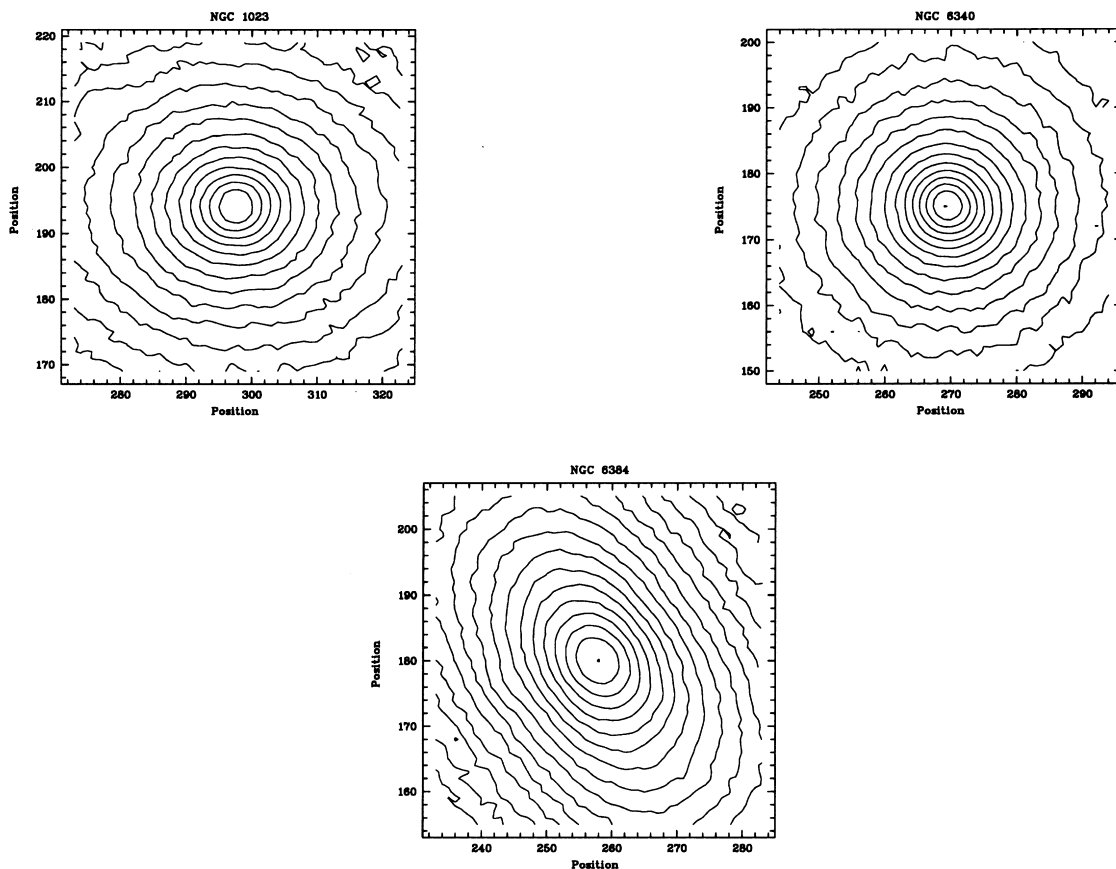


Figure 3. *I*-band isophotal maps of the central regions of the sample galaxies (continued).



**Figure 4.** *I*-band isophotal maps of the central regions of the sample galaxies (continued).

Once these two values  $[I(R)_{\text{mean}}/I(I)_{\text{mean}}$  and  $I_c(\text{H}\alpha)/I_c(R)$ ] are found, the  $\text{H}\alpha$  continuum image is obtained as

$$I_c = \frac{R_{\text{mean}}}{I_{\text{mean}}} \frac{I_c(\text{H}\alpha)}{I_c(R)} I(I). \quad (5)$$

This continuum can be subtracted from the original image, thereby giving the  $\text{H}\alpha$ -line image.

Figs 5–7 show the  $\text{H}\alpha$ -line images obtained by means of the methods described above. An error in the initial estimate of the radial velocity of NGC 513 prevented us from obtaining the  $\text{H}\alpha$ -line image of this galaxy. NGC 1023 does not present any nuclear  $\text{H}\alpha$  emission. We did not obtain  $\text{H}\alpha$  frames from NGC 6384.

### 3.3 Notes to individual objects

**NGC 3227:** in Figs 1 and 5 the peak isophotes correspond to  $\mu_I = 13.9 \text{ mag arcsec}^{-2}$  and  $\mu_{\text{H}\alpha} = 30.37 \text{ mag arcsec}^{-2}$ . In both contour plots the isophotal increment is  $0.25 \text{ mag arcsec}^{-2}$ .

The *I*-band isophotes are very smooth, with a monotonous increase in ellipticity for radii  $r \gtrsim 5 \text{ arcsec}$ . The position angles of the isophotes also decrease gradually from  $\text{PA} \approx 65^\circ$  at the centre to  $\text{PA} \approx 0^\circ$  at  $r \approx 2 \text{ arcsec}$ , changing abruptly to values  $\text{PA} \approx 160^\circ$  at larger radii. This is probably the position of the bar, although we cannot see it clearly in our images. Outside the represented region in Fig. 1, the galaxy shows a very distorted geometry, probably due to the interaction with its companion galaxy NGC 3226.

The line-emitting region is oriented at  $\text{PA} \approx 34^\circ$ . The nuclear region is very compact, with  $\text{FWHM} \approx 1.76 \text{ arcsec}$ , but probably

resolved since the estimated seeing for this observations is  $\text{FWHM} \approx 1.3 \text{ arcsec}$ . VLA data from Ulvestad, Wilson & Sramek (1981) and Ulvestad & Wilson (1984) show a partially resolved nuclear radio source of similar size (about 300 pc).

**NGC 3516:** in Figs 1 and 5 the peak isophotes correspond to  $\mu_I = 14.91 \text{ mag arcsec}^{-2}$  and  $\mu_{\text{H}\alpha} = 31.82 \text{ mag arcsec}^{-2}$ . In the *I*-band plot the isophotal increment is  $0.25 \text{ mag arcsec}^{-2}$ , while in the  $\text{H}\alpha$  one the increment is  $0.2 \text{ mag arcsec}^{-2}$ .

The stellar continuum contours are quite circular in the centre, but gain ellipticity as they progress outwards until  $r \approx 9 \text{ arcsec}$  due to the presence of a bar at  $\text{PA} \approx 173^\circ$ .

Two components are observed in the emission-line maps: an unresolved nuclear component and an extended component. The latter is oriented at  $\text{PA} \approx 45^\circ$ , with a total extension of about 12 arcsec, i.e., 2.7 kpc. The observed  $\text{H}\alpha$  emission morphology is very similar to that shown by Pogge (1989a). VLA observations from Wrobel & Heeschen (1988) reveal extended radio emission at  $\text{PA} \sim 45^\circ$ , i.e., aligned with the stellar continuum.

**NGC 3998:** in Figs 1 and 5 the peak isophotes correspond to  $\mu_I = 14.0 \text{ mag arcsec}^{-2}$  and  $\mu_{\text{H}\alpha} = 31.5 \text{ mag arcsec}^{-2}$ . In both contour plots the isophotal increment is  $0.5 \text{ mag arcsec}^{-2}$ .

The *I* isophotes are quite regular, with ellipticities  $\epsilon \leq 0.2$ ; the  $\text{H}\alpha$  contours are rounded, and the emitting region is barely resolved, with  $\text{FWHM} \approx 1.95 \text{ arcsec}$ .

**NGC 7469:** in Figs 1 and 5 the peak isophotes correspond to  $\mu_I = 14.4 \text{ mag arcsec}^{-2}$  and  $\mu_{\text{H}\alpha} = 30.35 \text{ mag arcsec}^{-2}$ . In both contour plots the isophotal increment is  $0.5 \text{ mag arcsec}^{-2}$ .

The represented *I*-band contours are slightly smoothed in order to filter out an error in the tracking of the telescope. However, the

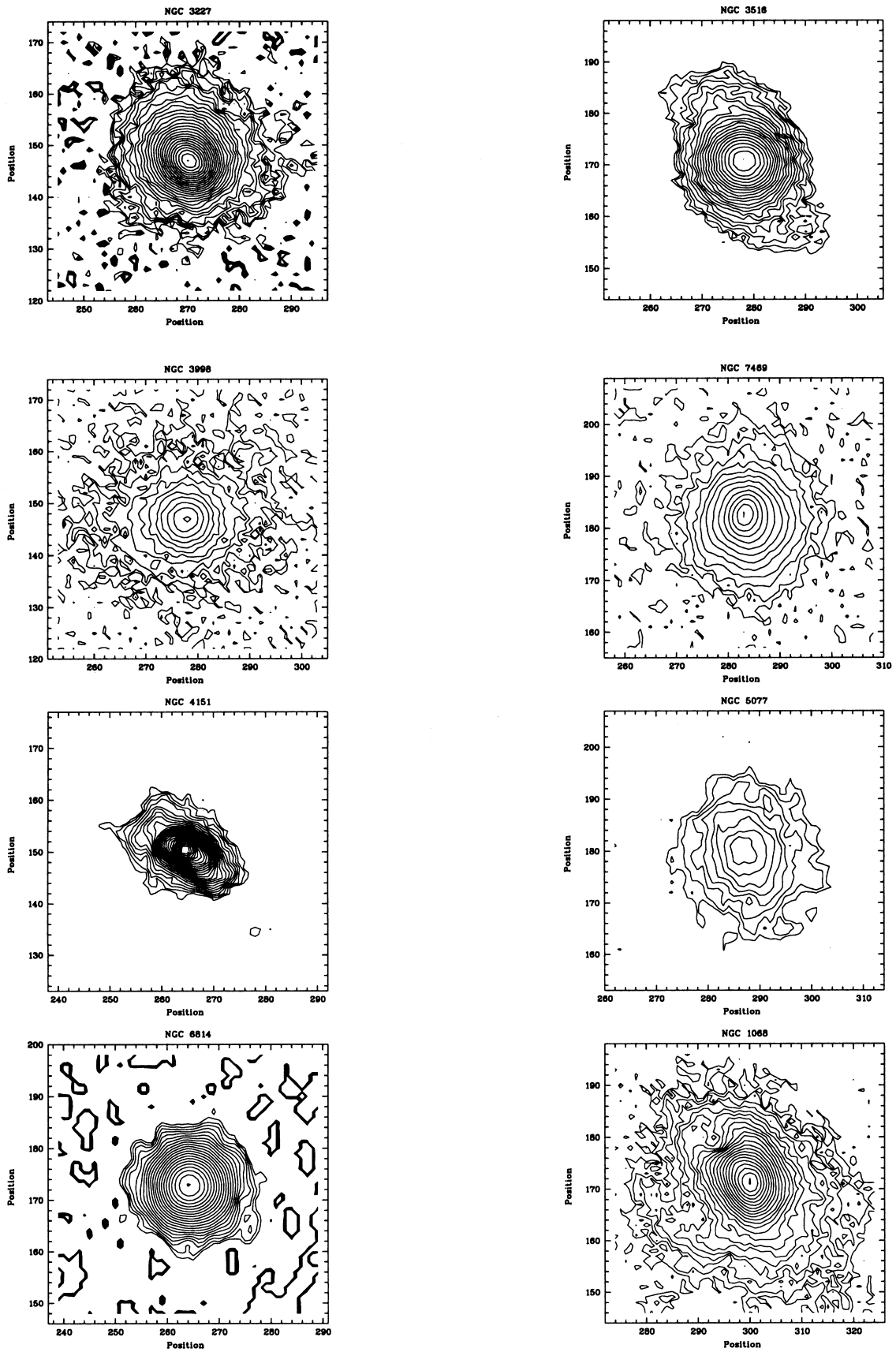


Figure 5. H $\alpha$  isophotal maps of the central regions of the sample galaxies.

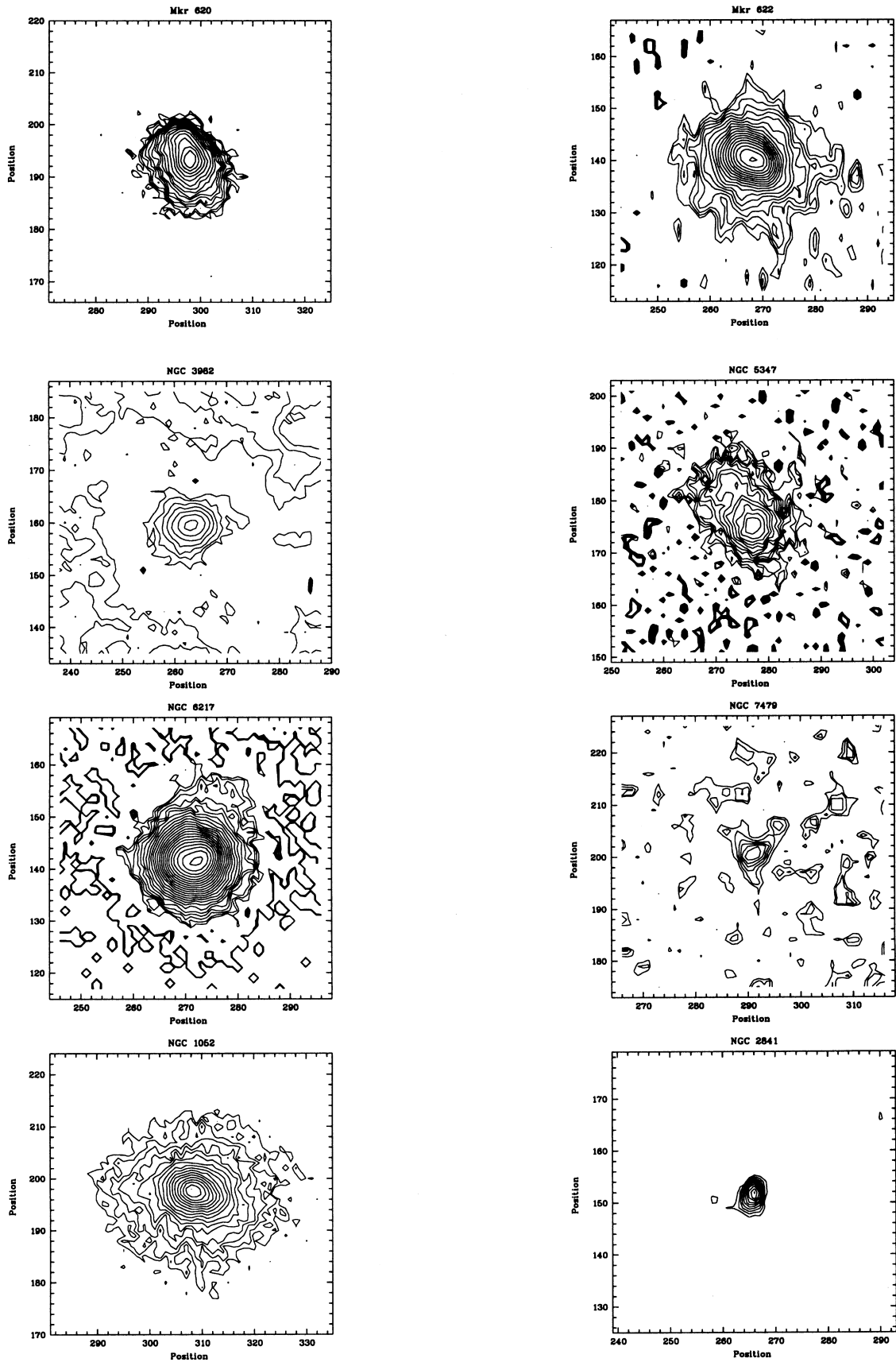


Figure 6. H $\alpha$  isophotal maps of the central regions of the sample galaxies (continued).

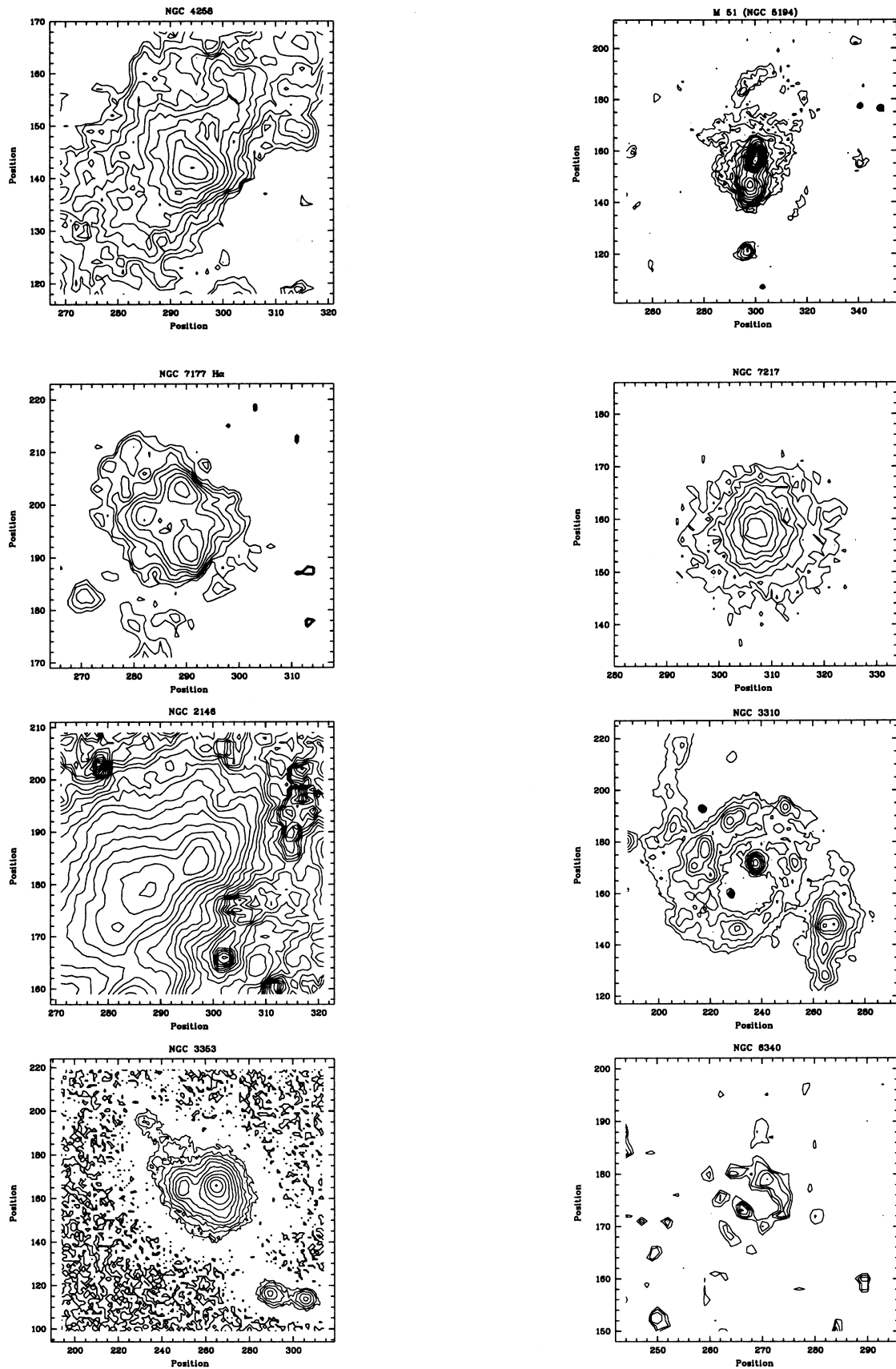


Figure 7.  $H\alpha$  isophotal maps of the central regions of the sample galaxies (continued).

observed displacement between the nucleus and the galaxy at  $PA \approx 115^\circ$  is real. This has also been reported by Márquez & Moles (1994), but while they measure a displacement of about 15 arcsec, our data show a maximum displacement of only 4 arcsec.

The  $H\alpha$  contours are roundish, and the region is partially resolved, with  $FWHM \approx 1.86$  arcsec.

**NGC 4151:** in Figs 1 and 5 the peak isophotes correspond to  $\mu_I = 13.1 \text{ mag arcsec}^{-2}$  and  $\mu_{H\alpha} = 27.27 \text{ mag arcsec}^{-2}$ . In both contour plots the isophotal increment is  $0.25 \text{ mag arcsec}^{-2}$ .

While  $I$ -band isophotes are almost circular (only a very little elongation with  $\epsilon \approx 0.04$  and  $PA \approx 50^\circ$  can be observed for radius greater than 6 arcsec), the emission-line contours are extended and notably elongated at  $PA \approx 50^\circ$ . An outstanding difference is observed between the  $V$ - and  $R$ -band isophote shapes, which follow closely the emission-line distribution, and the  $I$ -band map, virtually free from emission-line contamination. All these maps are described in detail in Terlevich et al. (1991).

**NGC 5077:** in Fig. 1 the peak isophote in the  $I$ -band map corresponds to  $\mu_I = 15.72 \text{ mag arcsec}^{-2}$ , with isophotal increments of  $0.25 \text{ mag arcsec}^{-2}$ . The  $H\alpha$  map shown in Fig. 5 is represented in logarithmic instrumental units.

This is an elliptical galaxy oriented at  $PA \approx 10^\circ$  and all the  $I$ -band isophotes, except the innermost ones, have the same orientation.

The line-emitting region is roughly circular and resolved, with  $FWHM \approx 3.13$  arcsec.

**NGC 6814:** in Figs 1 and 5 the peak isophotes correspond to  $\mu_I = 15.84 \text{ mag arcsec}^{-2}$  and  $\mu_{H\alpha} = 33.58 \text{ mag arcsec}^{-2}$ . In both contour plots the isophotal increment is  $0.25 \text{ mag arcsec}^{-2}$ .

The ellipticity of the isophotes in the  $I$ -band map changes from  $\epsilon = 0$  in the nucleus to  $0.2$  at  $r \approx 6$  arcsec. At this point the position angle is  $PA \approx 20^\circ$ , which corresponds to the orientation of the bar in NGC 6814.

During the 1988 run, when the images were obtained, the nucleus was experiencing a period of minimum activity (E. Pérez, private communication) and we were able to produce the  $H\alpha$ -line map by subtracting a pseudo-continuum estimated from the  $I$  band. The  $H\alpha$  shows a compact region whose size  $FWHM \approx 2.13$  arcsec is nearly equal to the seeing disc.

**NGC 513:** in Fig. 1 the peak isophotes correspond to  $\mu_I = 15.7 \text{ mag arcsec}^{-2}$ . The isophotal increment is  $0.25 \text{ mag arcsec}^{-2}$ . This galaxy does not have a morphological classification in the catalogues. The inner  $I$ -band isophotes are roundish, but their ellipticity increases up to  $\epsilon \approx 0.4$  at  $r \approx 5$  arcsec. Their elongated shape indicate the presence of a bar at  $PA \approx 115^\circ$ . The abrupt change in the position angle at this point from  $PA \approx 115^\circ$  to  $69^\circ$ , which is the position angle of the galaxy as a whole, is also strong evidence for the existence of a bar (see next sections), as is the small bump seen in the surface brightness profile. In the outer regions, faint spiral arms tightly bound to the bulge might be present. We propose that this galaxy be classified as SAB(r)a.

**NGC 1068:** in Figs 2 and 5 the peak isophotes correspond to  $\mu_I = 13.48 \text{ mag arcsec}^{-2}$  and  $\mu_{H\alpha} = 28.35 \text{ mag arcsec}^{-2}$ . In the  $I$ -band plot the isophotal increment is  $0.2 \text{ mag arcsec}^{-2}$ , while in the  $H\alpha$  one the increment is  $0.25 \text{ mag arcsec}^{-2}$ .

The inner isophotes of the stellar continuum map gain ellipticity from the centre to  $r \approx 12$  arcsec, where they reach  $\epsilon \approx 0.4$  at  $PA \approx 60^\circ$ . From this point on, the ellipticity decreases again. This maximum in the radial variation of the ellipticity and the oval shape that the isophotes adopt lead us to reclassify this galaxy as SAB. The full image of the galaxy (not shown here) shows that the

spiral arms departure from the bar at  $PA \approx 60^\circ$ . This feature has not been observed in photographic plates (e.g. Kodaira, Okamura & Ichikawa 1990), since the bulge of the galaxy is usually overexposed due to the steep inner surface brightness profile.

Along with NGC 4151, this is one of the few galaxies in our sample whose  $V$  and  $R$  contour maps differ substantially from the  $I$ -band one. While in  $I$  the inner isophotes are quite circular, in  $V$  and  $R$  they present elongations. This behaviour of the  $V$  and  $R$  maps can be also explained by strong emission-line contamination.

The emission-line map shows a very extended region. The central zone is compact but resolved, and oriented at  $PA \sim 0^\circ$  to  $18^\circ$ .

**Mrk 620:** in Figs 2 and 6 the peak isophotes correspond to  $\mu_I = 15.44 \text{ mag arcsec}^{-2}$  and  $\mu_{H\alpha} = 31.51 \text{ mag arcsec}^{-2}$ . In both contour plots the isophotal increment is  $0.25 \text{ mag arcsec}^{-2}$ . In the  $I$ -band map, the position angle of the isophotes change from  $PA \approx 10^\circ$  at the centre to  $PA \approx 110^\circ$  at  $r \approx 9$  arcsec. This is the position of the bar.

The  $H\alpha$  region is resolved and elongated at  $PA \approx 10^\circ$ .

**Mrk 622:** in Figs 2 and 6 the peak isophotes correspond to  $\mu_I = 15.96 \text{ mag arcsec}^{-2}$  and  $\mu_{H\alpha} = 34 \text{ mag arcsec}^{-2}$ . In the  $I$ -band plot the isophotal increment is  $0.25 \text{ mag arcsec}^{-2}$ , while in the  $H\alpha$  one the increment is  $0.2 \text{ mag arcsec}^{-2}$ .

MacKenty (1990) classifies this galaxy as SO/a, considering it an amorphous galaxy, possibly with spiral structure. Although the galaxy has a disc, we have not been able to detect any spiral pattern, even after masking the nucleus. This is why we consider this object a lenticular galaxy. The variation of the ellipticity from  $\epsilon \approx 0.28$  at  $r \approx 4$  arcsec to  $\epsilon \approx 0.34$  at  $r \approx 12$  arcsec (as well as the twisting of the position angle at the same distances), and its subsequent monotonical fall until  $\epsilon \approx 0.1$  at the outermost radii could be the signature of a bar. This leads us to suggest a reclassification of this galaxy as SBO.

Extended line emission at  $PA \sim 45^\circ$  is observed, but the small angular size of the object, the relatively poor seeing ( $FWHM \approx 1.95$  arcsec) and the uncertainties involved in the continuum subtraction process make the estimation of the linear size of the region difficult. A Gaussian fit to the emitting region gives a value of  $FWHM \approx 2.1$  arcsec, slightly larger than the seeing disc.

**NGC 3982:** in Figs 2 and 6 the peak isophotes correspond to  $\mu_I = 16.2 \text{ mag arcsec}^{-2}$  and  $\mu_{H\alpha} = 34.5 \text{ mag arcsec}^{-2}$ . In the  $I$ -band plot the isophotal increment is  $0.25 \text{ mag arcsec}^{-2}$ , while in the  $H\alpha$  one the increment is  $0.5 \text{ mag arcsec}^{-2}$ .

The stellar continuum map shows that the isophotes are oriented at  $PA \approx 20^\circ$ , and their ellipticity changes monotonically from  $\epsilon \approx 0.1$  to  $0.35$  at  $r \approx 6$  arcsec with  $PA \approx 0^\circ$ . This can be considered the position of the bar.

The line-emitting region is unresolved. A ring composed by  $H II$  regions is observed at the edge of the area shown in the  $H\alpha$  map.

**NGC 5347:** in Figs 2 and 6 the peak isophotes correspond to  $\mu_I = 19.09 \text{ mag arcsec}^{-2}$  and  $\mu_{H\alpha} = 35 \text{ mag arcsec}^{-2}$ . In both contour plots the isophotal increment is  $0.25 \text{ mag arcsec}^{-2}$ .

The  $I$ -band isophotes are oriented at  $PA \approx 97^\circ$ , which corresponds to the orientation of the bar. The ellipticity changes monotonically from  $\epsilon \approx 0.1$  at the centre to  $0.5$  at  $r \approx 17$  arcsec due to the presence of the bar.

The  $H\alpha$  nuclear emission region is extended and asymmetrically oriented at  $PA \approx 40^\circ$ . Its total angular size is about 6 arcsec, very similar to that measured by Pogge (1989a).

**NGC 6217:** in Figs 2 and 6 the peak isophotes correspond to  $\mu_I = 14.61 \text{ mag arcsec}^{-2}$  and  $\mu_{H\alpha} = 31.6 \text{ mag arcsec}^{-2}$ . In the

*I*-band plot the isophotal increment is  $0.3 \text{ mag arcsec}^{-2}$ , while in the  $H\alpha$  one the increment is  $0.25 \text{ mag arcsec}^{-2}$ .

The stellar continuum map shows isophotes oriented at  $PA \approx 150^\circ$ , which is the orientation of its prominent bar.

The emission-line map shows a resolved nuclear region of  $\text{FWHM} \sim 2.1 \text{ arcsec}$ .

**NGC 7479:** in Figs 2 and 6 the peak isophotes correspond to  $\mu_I = 16.31 \text{ mag arcsec}^{-2}$  and  $\mu_{H\alpha} = 34.5 \text{ mag arcsec}^{-2}$ . In both contour plots the isophotal increment is  $0.2 \text{ mag arcsec}^{-2}$ .

The stellar continuum images reveal a small bulge whose isophotes are oriented at  $PA \approx 40^\circ$ . This angle varies subsequently until  $PA \approx 13^\circ$ , which is the position of the bar. The isophotes are deformed to the NS due to the presence of dust in the bar.

The nuclear line-emitting region is small but resolved, with a total size of about  $3 \text{ arcsec}$  ( $630 \text{ pc}$ ) and elongated at  $PA \approx 120^\circ$ .

**NGC 1052:** in Figs 2 and 6 the peak isophotes correspond to  $\mu_I = 14.61 \text{ mag arcsec}^{-2}$  and  $\mu_{H\alpha} = 31.02 \text{ mag arcsec}^{-2}$ . In both contour plots the isophotal increment is  $0.25 \text{ mag arcsec}^{-2}$ .

The isophotes in *I*-band are oriented at the same position angle as the whole galaxy,  $PA \approx 113^\circ$ .

The  $H\alpha$  line-emitting region is resolved ( $\text{FWHM} \approx 1.93 \text{ arcsec}$ ) and elongated at  $PA \approx 69^\circ$ . The total angular size is about  $12 \text{ arcsec}$ , smaller than the size derived by Fosbury et al. (1978) of about  $20 \text{ arcsec}$ .

**NGC 2841:** in Figs 3 and 6 the peak isophotes correspond to  $\mu_I = 13.9 \text{ mag arcsec}^{-2}$  and  $\mu_{H\alpha} = 34.0 \text{ mag arcsec}^{-2}$ . In the *I*-band plot the isophotal increment is  $0.25 \text{ mag arcsec}^{-2}$ , while in the  $H\alpha$  one the increment is  $0.2 \text{ mag arcsec}^{-2}$ .

The stellar continuum isophotes are very regular and oriented at  $PA \approx 150^\circ$ , which is the general orientation of the galaxy. The precession of about  $10^\circ$  from  $r \approx 10 \text{ arcsec}$  to  $r \approx 32 \text{ arcsec}$  in the position angle of the isophotes attributed by Varela (1992) to a triaxial bulge is not observed in our *I*-band images, although it is indeed present in the *V* and *R* bands.

The small line-emitting region is elongated at  $PA \approx 146^\circ$ . The region is resolved in the direction of elongation, but not in the orthogonal one.

**M106 (NGC 4258):** in Figs 3 and 7 the peak isophotes correspond to  $\mu_I = 14.25 \text{ mag arcsec}^{-2}$  and  $\mu_{H\alpha} = 35.0 \text{ mag arcsec}^{-2}$ . In the *I*-band plot the isophotal increment is  $0.25 \text{ mag arcsec}^{-2}$ , while in the  $H\alpha$  one the increment is  $0.2 \text{ mag arcsec}^{-2}$ .

The *I*-band map shows a dust band crossing the frame near the nucleus in the direction NW to SE. Apart from this obvious distortion, the isophotes are quite regular and oriented at  $PA \approx 150^\circ$ . The ellipticity increases monotonically from values  $\epsilon = 0.1$  in the centre to  $\epsilon = 0.6$  at  $r \approx 12 \text{ arcsec}$ , where it reaches a maximum; at  $r \approx 20 \text{ arcsec}$ , the ellipticity decreases abruptly to values around  $\epsilon = 0.4$  (see Fig. 16). The variation of the ellipticity reflects the behaviour of the bar, whose maximum radius is about  $r \approx 20 \text{ arcsec}$ .

In the  $H\alpha$  map we observe extended emission oriented at  $PA \approx 135^\circ$  and an unresolved compact nuclear region. The overall size of the emitting region is about  $4.5$  to  $6 \text{ arcsec}$ .

**M51 (NGC 5194):** in Figs 3 and 7 the peak isophotes correspond to  $\mu_I = 14.5 \text{ mag arcsec}^{-2}$  and  $\mu_{H\alpha} = 32.4 \text{ mag arcsec}^{-2}$ . In the *I*-band plot the isophotal increment is  $0.25 \text{ mag arcsec}^{-2}$ , while in the  $H\alpha$  one the increment is  $0.2 \text{ mag arcsec}^{-2}$ .

The inner isophotes of the *I*-band map are elongated at  $PA \approx 0^\circ$ . These are the signature of a small bulge. From  $r \approx 3 \text{ arcsec}$  onwards the isophotes become irregular due to the presence of dusty spiral arms.

The following features are observed in the  $H\alpha$  map: (a) a

nuclear region elongated at  $PA \approx 167^\circ$  and partially resolved; (b) a round region with a diameter of about  $3 \text{ arcsec}$  ( $37 \text{ pc}$ ) located to the SE of the nuclear region; and (c) a fainter ring-shaped structure located to the NW of diameter  $8.5 \text{ arcsec}$  ( $104 \text{ pc}$ ). These  $H\alpha$  structures are aligned in the direction of the nuclear elongation, and match those observed by Ford et al. (1985).

**NGC 7177:** in Figs 3 and 7 the peak isophotes correspond to  $\mu_I = 15.72 \text{ mag arcsec}^{-2}$  and  $\mu_{H\alpha} = 35.5 \text{ mag arcsec}^{-2}$ . In the *I*-band plot the isophotal increment is  $0.25 \text{ mag arcsec}^{-2}$ , while in the  $H\alpha$  one the increment is  $0.2 \text{ mag arcsec}^{-2}$ . The *I*-band map shows a progressive elongation of the isophotes until they are aligned at  $PA \approx 20^\circ$ , which corresponds to the bar position angle.

The line-emitting region is resolved in several nodes ( $HII$  regions) that compose a pseudo-ring (Alvarez Alvarez 1997), but there is not a neat nuclear region. The  $H\alpha$  image from Pogge (1989b) shows a stellar nucleus that is not present in our images, as well as the individual  $HII$  regions without a specific distribution pattern.

**NGC 7217:** in Figs 3 and 7 the peak isophotes correspond to  $\mu_I = 14.88 \text{ mag arcsec}^{-2}$  and  $\mu_{H\alpha} = 32.31 \text{ mag arcsec}^{-2}$ . In both contour plots the isophotal increment is  $0.2 \text{ mag arcsec}^{-2}$ .

The *I*-band isophotes are very circular and regular ( $\epsilon \lesssim 0.1$ ), aligned at  $PA \approx 75^\circ$ .

The  $H\alpha$  line-emitting region is extended with a total size of about  $9 \text{ arcsec}$  ( $112 \text{ pc}$ ).

**NGC 2146:** in Figs 3 and 7 the peak isophotes correspond to  $\mu_I = 16.2 \text{ mag arcsec}^{-2}$  and  $\mu_{H\alpha} = 33.4 \text{ mag arcsec}^{-2}$ . In both contour plots the isophotal increment is  $0.2 \text{ mag arcsec}^{-2}$ .

The *I*-band isophotes are very irregular, revealing a dust lane which crosses the galaxy from NW to SE at  $PA \approx 130^\circ$ .

The  $H\alpha$  nuclear line emission is extended. A big  $HII$  region is observed SE of the nucleus.

**NGC 3310:** in Figs 3 and 7 the peak isophotes correspond to  $\mu_I = 14.5 \text{ mag arcsec}^{-2}$  and  $\mu_{H\alpha} = 31.5 \text{ mag arcsec}^{-2}$ . The isophotal increment is  $0.25 \text{ mag arcsec}^{-2}$  in the *I*-band plot and  $0.5 \text{ mag arcsec}^{-2}$  in the  $H\alpha$  one; the size of the plots has been enlarged to  $33 \times 33 \text{ arcsec}^2$  in order to show the outstanding circumnuclear ring.

The *I*-band map shows a compact centre, which corresponds to the small bulge of the galaxy. Outside this region of about  $5 \text{ arcsec}$ , the isophotes reveal the positions of the stars in the circumnuclear ring. We can see that the stellar nucleus is the centre of symmetry of the stellar distribution. On the other hand, the  $H\alpha$  map shows an unresolved nuclear region and a circumnuclear ring elongated at  $PA \approx 140^\circ$ , whose centre is displaced about  $2.7 \text{ arcsec}$  to the SE of the stellar nucleus. To the SW and NE, two spiral arms arise tangent to the ring. At the beginning of the SW arm, a giant  $HII$  region is observed. This region is resolved into two components. It has been suggested that this region is the result of a merger (Schweizer 1983).

**NGC 3353:** in Figs 3 and 7 the peak isophotes correspond to  $\mu_I = 17.4 \text{ mag arcsec}^{-2}$  and  $\mu_{H\alpha} = 31.7 \text{ mag arcsec}^{-2}$ . In both contour plots the isophotal increment is  $0.5 \text{ mag arcsec}^{-2}$ . The size of the plots has been enlarged to  $33 \times 33 \text{ arcsec}^2$  in order to show all the extranuclear sources.

The galaxy shows merger structures. In the *I*-band image the centre comprises a strong source to the NW, and two more sources to the S and NE. The latter two sources are stronger in the *R*-band map, where more regions are observed further away to the SW. These two regions are located in the isophotal tail of the *I*-band map. Except for these prominent features the overall pattern of the isophotes is rather regular, and they are oriented at  $PA \approx 45^\circ$ .

Several resolved regions are observed in the  $H\alpha$  map: an intense source located to the NW of the centre, a fainter source located to the NE, and two more sources at the bottom right corner of the map. An additional source, that may correspond to the symmetry centre of the underlying stellar distribution and is clearly observed in our broad-band images (Sánchez-Portal 1996), and in particular in the  $I$ -band one, is not detected in the  $H\alpha$  frame.

**NGC 1023:** in Fig. 4 the peak isophotes correspond to  $\mu_I = 13.85 \text{ mag arcsec}^{-2}$ . The isophotal increment is  $0.25 \text{ mag arcsec}^{-2}$ .

The stellar continuum presents regular isophotes which increase monotonically their ellipticity towards the outer regions due to the presence of a bar.

**NGC 6340:** in Figs 4 and 7 the peak isophotes correspond to  $\mu_I = 15.22 \text{ mag arcsec}^{-2}$  and  $\mu_{H\alpha} = 35.9 \text{ mag arcsec}^{-2}$ . The isophotal increment is  $0.25 \text{ mag arcsec}^{-2}$  in the  $I$ -band plot and  $0.2 \text{ mag arcsec}^{-2}$  in the  $H\alpha$  one.

The  $I$ -band isophotes are nearly circular with an overall inclination of  $PA \approx 23^\circ$ .

A very weak extranuclear emission is observed in  $H\alpha$ . The spectrum from Ho et al. (1995) in this position shows a weak  $[N II]$  feature.

**NGC 6384:** in Fig. 4 the peak isophotes correspond to  $\mu_I = 16.12 \text{ mag arcsec}^{-2}$ . The isophotal increment is  $0.2 \text{ mag arcsec}^{-2}$ .

The stellar continuum image presents very regular elongated isophotes at  $PA \approx 33^\circ$ , corresponding to the orientation of the bar.

### 3.4 Broad-band surface brightness and colour profiles

The analysis of the radial surface brightness variation of regular galaxies is based on the assumption that the isophotes can be represented by a series of nested ellipses. Therefore each point of the profile can be determined by the ellipse semi-axis and the surface brightness value along the ellipse.

We have obtained the azimuthally averaged surface brightness profiles from the broad-band  $VRI$  images using the program PROF described by Davies et al. (1985). This program makes use of an initial guess of ellipse centre, ellipticity and position angle, and assuming that the azimuthal variation of the surface brightness is a periodic function, this can therefore be expressed as a Fourier series  $I(\phi) = I_0 + \sum_{n=1}^4 (A_n \sin n\phi + B_n \cos n\phi)$ . The program calculates the coefficients of the series using a least-squares minimization technique.

The profile errors have been computed taking into account the source photon noise, the sky value error and the CCD readout noise, according to the equation (Granato et al. 1993)

$$\frac{\sigma_{(I)}^2}{\langle I \rangle^2} = \frac{\bar{n}_e + \sigma_{\text{ron}}^2}{N_{\text{ring}}(\bar{n}_e + \bar{n}_e)^2} + \frac{\bar{n}_{\text{bk}} + \sigma_{\text{ron}}^2}{N_{\text{bk}}(\bar{n}_e + \bar{n}_e)^2} + \frac{\sigma_{\text{bk}}^2}{(\bar{n}_e + \bar{n}_e)^2}, \quad (6)$$

where  $N_{\text{ring}}$  and  $N_{\text{bk}}$  are, respectively, the number of pixels contained in the ring used for profile calculation and in the region used for sky computation,  $\bar{n}_e$  is the mean electron count in the ring pixels,  $\bar{n}_{\text{bk}}$  is the mean electron count from the background,  $\sigma_{\text{bk}}$  is the background error, and  $\sigma_{\text{ron}}$  is the CCD readout noise.

Figs 8–20 show the surface brightness profiles<sup>4</sup> (not corrected for inclination), the radial variation of ellipticity and position

<sup>4</sup>We have adopted the equivalent radius, introduced by de Vaucouleurs et al. (1976; Second Reference Catalog) and defined by  $r_{\text{eq}} = \sqrt{a/\pi}$ , where  $a$  is the area enclosed by the isophote, i.e., the radius of the circle whose area is equal to that of the isophote.

angle, and the  $R - I$  and  $V - I$  colour profiles for the sample objects. The colour profiles have been computed subtracting the surface brightness profiles. In a few cases, generally related to the presence of bars, some irregularities are observed in the colour profiles. These are most likely due to artefacts in the surface brightness profile interpolation. All the data can be obtained by anonymous ftp at `astro1.ft.uam.es`

The position angles and inclinations of the sample galaxies have been derived by averaging these parameters among the outermost valid ellipses fitted to each frame through the PROF program. The final values adopted, presented in Table 4, have been obtained as the mean of the results for each of the three broad-band filters. The inclination value of NGC 4151 has been taken from Simkin (1975), as the position of our outermost isophotes ( $PA \approx 130^\circ$ ) does not correspond to the position angle of the disc but of a bar. The surface brightness profile of NGC 7479 is dominated also by the strong bar, therefore preventing us from obtaining accurate values of position angle and inclination. We did not attempt to obtain azimuthally averaged profiles of the irregular galaxy NGC 3353.

The derived values of inclination can be used to correct the surface brightness profile, as well as all derived morphological parameters:

$$\mu_{\text{real}} = \mu_{\text{obs}} - 2.5 \log(1 - \epsilon), \quad (7)$$

where  $1 - \epsilon = b/a = \cos i$ , and  $b$  and  $a$  are, respectively, the semimajor and semiminor axes of the galaxy.

The broad-band images and profiles can be used to determine the existence of bars. We have applied the following criteria. (a) The bar is seen in the broad-band images. (b) The ellipticity presents a maximum (or two maxima, in the case of double-barred galaxies) and then decreases to reveal the inclination of the disc; the position angle keeps roughly constant while the ellipticity is rising (Mulchaey, Regan & Kundu 1997). (c) There is either a

**Table 4.** Mean position angle and inclination of the sample galaxies.

Galaxy	PA ( $^\circ$ )	$i$ ( $^\circ$ )
NGC 3227	$150.2 \pm 1.8$	$63.6 \pm 0.7$
NGC 3516	$46.9 \pm 3.2$	$37.7 \pm 0.3$
NGC 3998	$136.5 \pm 1.3$	$37.4 \pm 0.7$
NGC 7469	$139.0 \pm 15.0$	$32.5 \pm 3.6$
NGC 4151	$26.0 \pm 3.5$	$21.0 \pm 5.0$
NGC 5077	$10.1 \pm 0.2$	$45.0 \pm 0.1$
NGC 6814	$113.0 \pm 10.0$	$22.5 \pm 1.2$
NGC 513	$69.3 \pm 1.2$	$54.8 \pm 2.9$
NGC 1068	$19.5 \pm 1.0$	$38.3 \pm 1.3$
Mrk 620 (NGC 2273)	$84.4 \pm 1.6$	$43.0 \pm 0.1$
Mrk 622	$41.3 \pm 10.0$	$26.0 \pm 1.7$
NGC 3982	$16.9 \pm 1.1$	$27.2 \pm 1.1$
NGC 5347	$117.5 \pm 0.9$	$38.2 \pm 1.4$
NGC 6217	$159.7 \pm 1.9$	$44.8 \pm 0.9$
NGC 7479	–	–
NGC 1052	$113.4 \pm 1.2$	$48.8 \pm 0.3$
NGC 2841	$149.7 \pm 1.9$	$59.0 \pm 0.9$
M106 (NGC 4258)	$161.6 \pm 2.6$	$55.9 \pm 0.7$
M51 (NGC 5194)	$143.2 \pm 0.9$	$26.2 \pm 3.4$
NGC 7177	$83.6 \pm 1.2$	$49.2 \pm 1.0$
NGC 7217	$75.8 \pm 6.5$	$28.7 \pm 0.6$
NGC 2146	$133.5 \pm 0.2$	$64.3 \pm 0.9$
NGC 3310	$176.8 \pm 4.3$	$35.9 \pm 0.8$
NGC 3353	–	–
NGC 1023	$78.2 \pm 3.5$	$60.4 \pm 5.3$
NGC 6340	$107.9 \pm 8.2$	$23.1 \pm 1.5$
NGC 6384	$32.9 \pm 2.7$	$37.4 \pm 4.7$

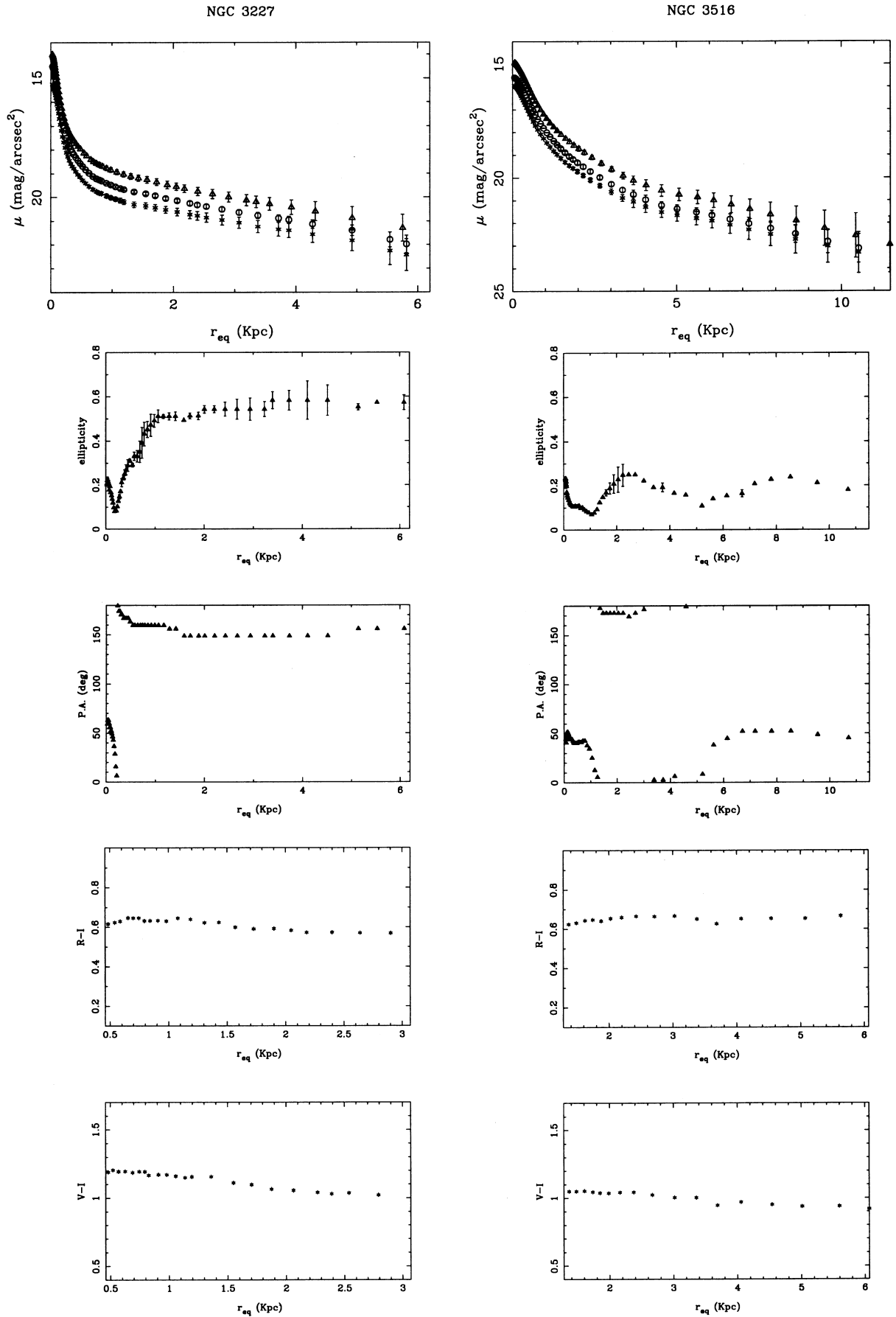


**Figure 8.** Top panel: surface brightness profiles in the V (\*), R (○) and I (Δ) bands; middle panels: I-band ellipticity and polar angle profiles; bottom panels: R – I and V – I colour profiles.

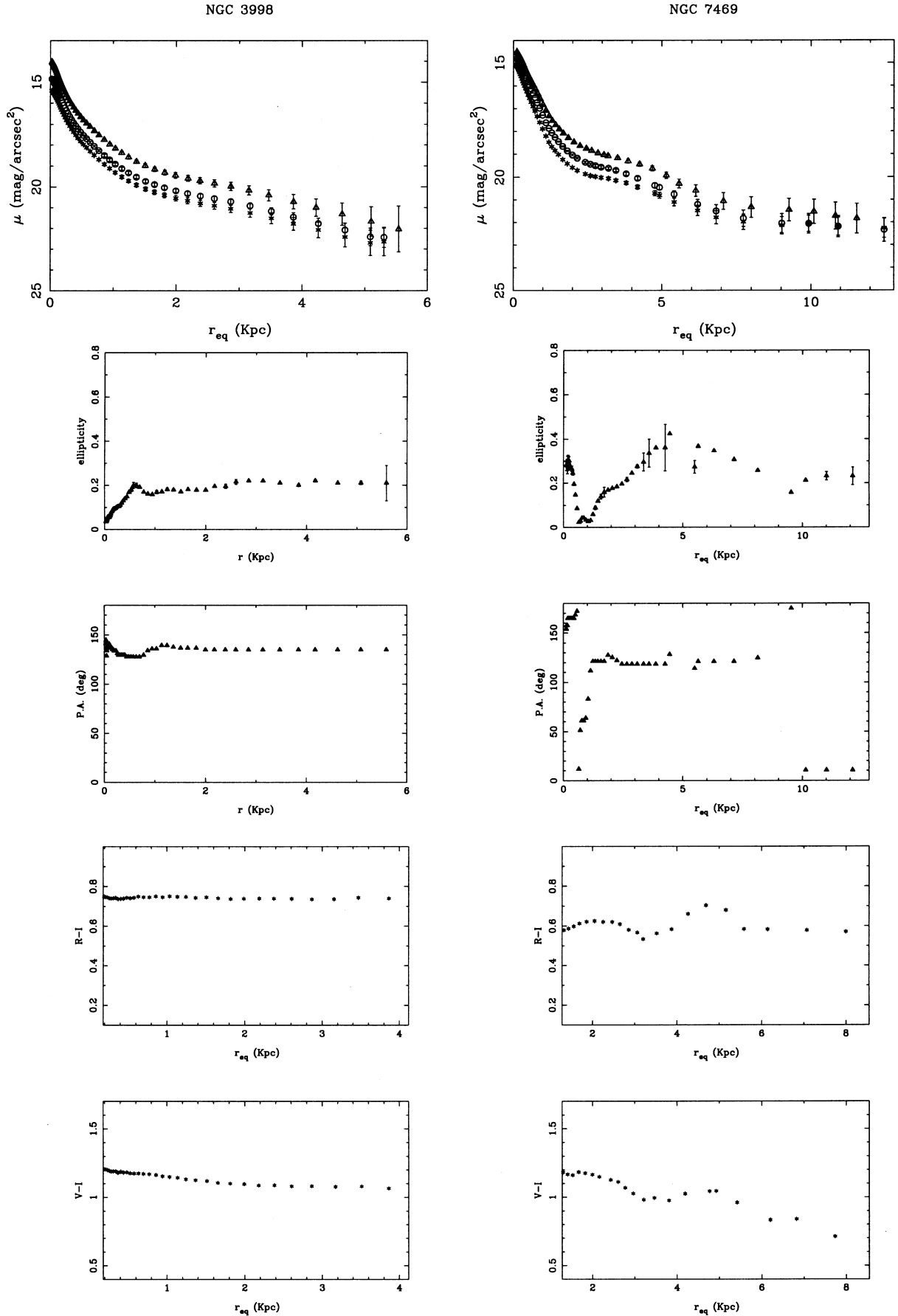


**Figure 9.** Top panel: surface brightness profiles in the V (\*), R (O) and I ( $\Delta$ ) bands; middle panels: I-band ellipticity and polar angle profiles; bottom panels: R – I and V – I colour profiles.

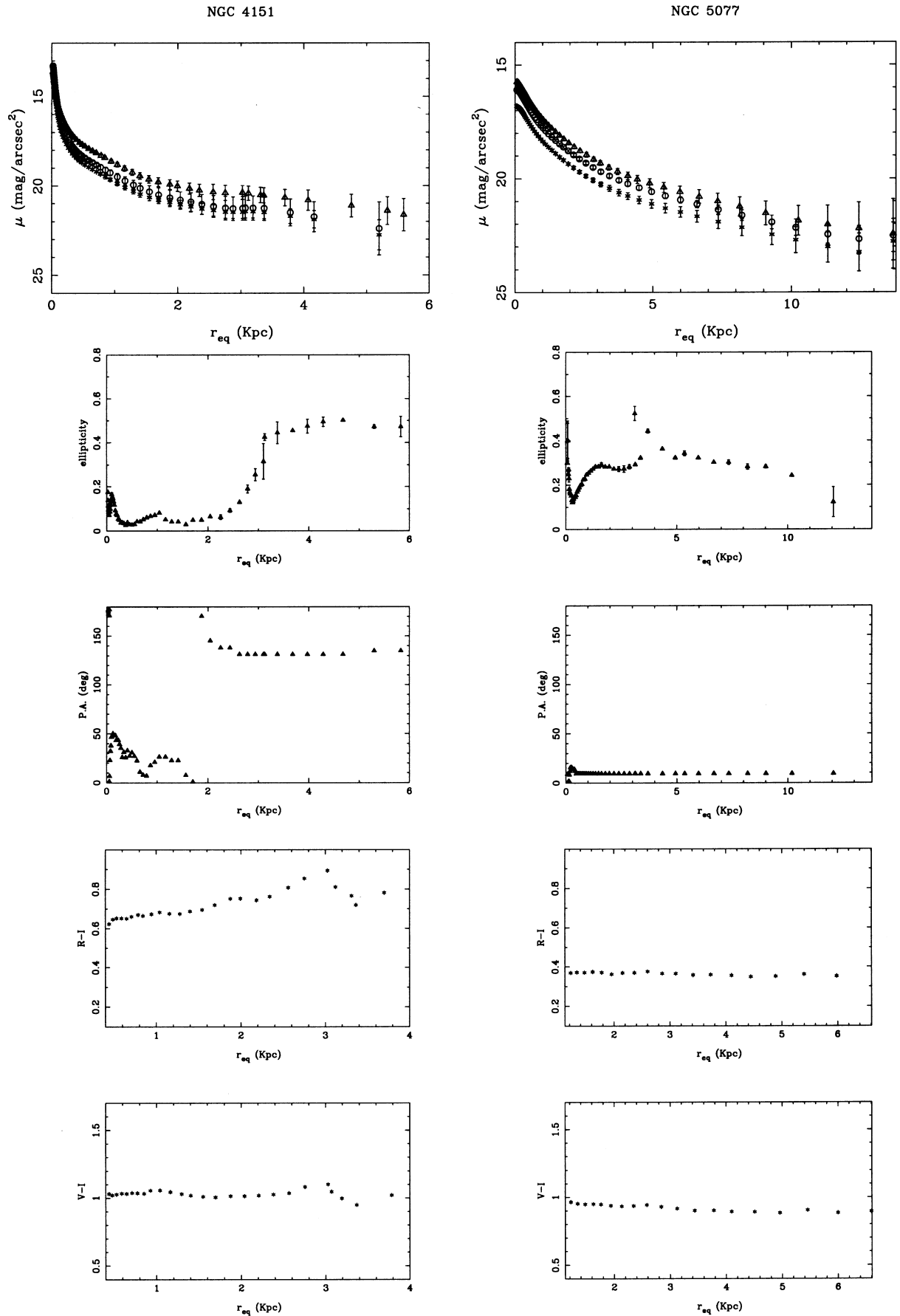


**Figure 10.** Top panel: surface brightness profiles in the  $V$  (\*),  $R$  (O) and  $I$  ( $\Delta$ ) bands; middle panels:  $I$ -band ellipticity and polar angle profiles; bottom panels:  $R-I$  and  $V-I$  colour profiles.

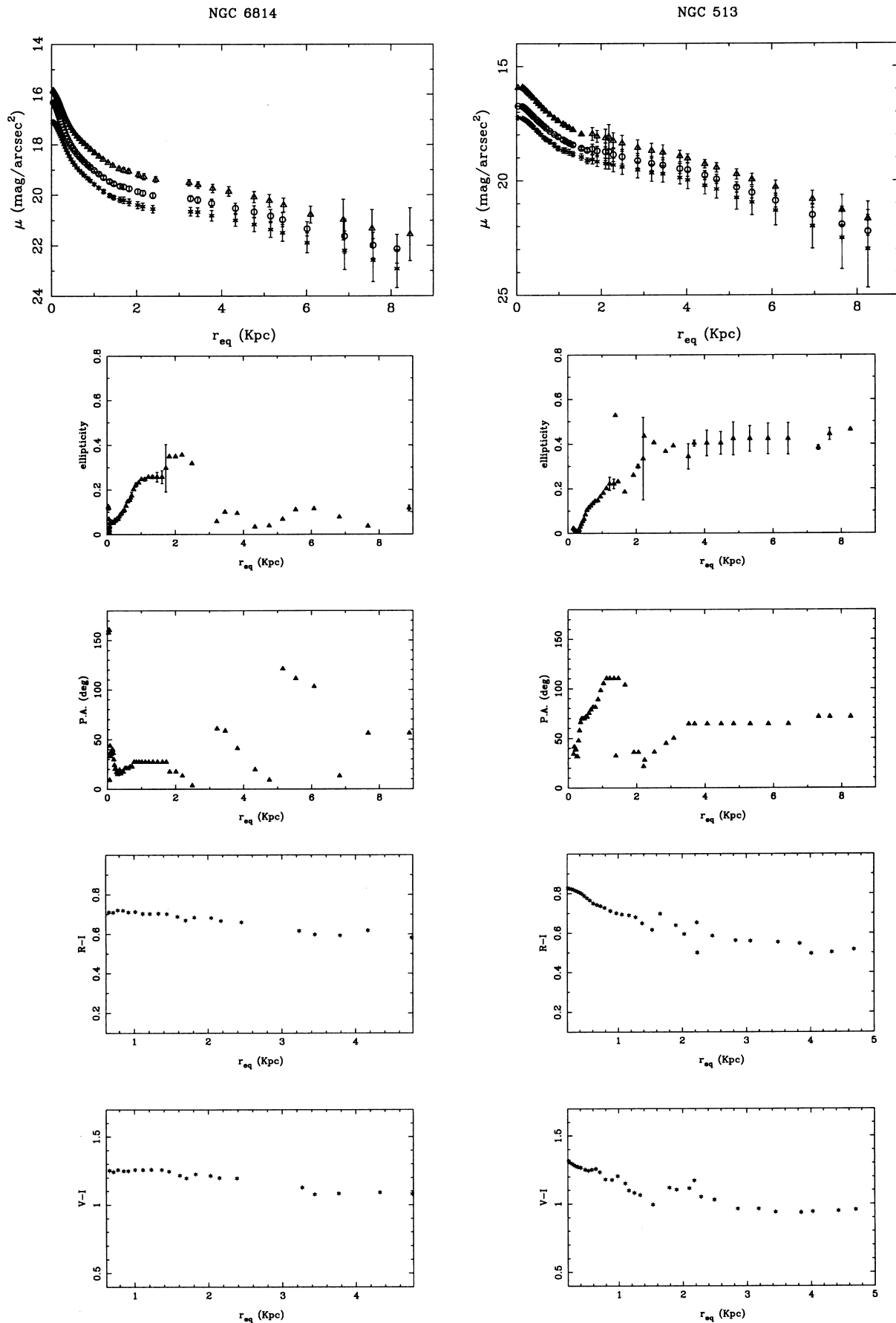


**Figure 11.** Top panel: surface brightness profiles in the  $V$  (\*),  $R$  ( $\circ$ ) and  $I$  ( $\triangle$ ) bands; middle panels:  $I$ -band ellipticity and polar angle profiles; bottom panels:  $R - I$  and  $V - I$  colour profiles.

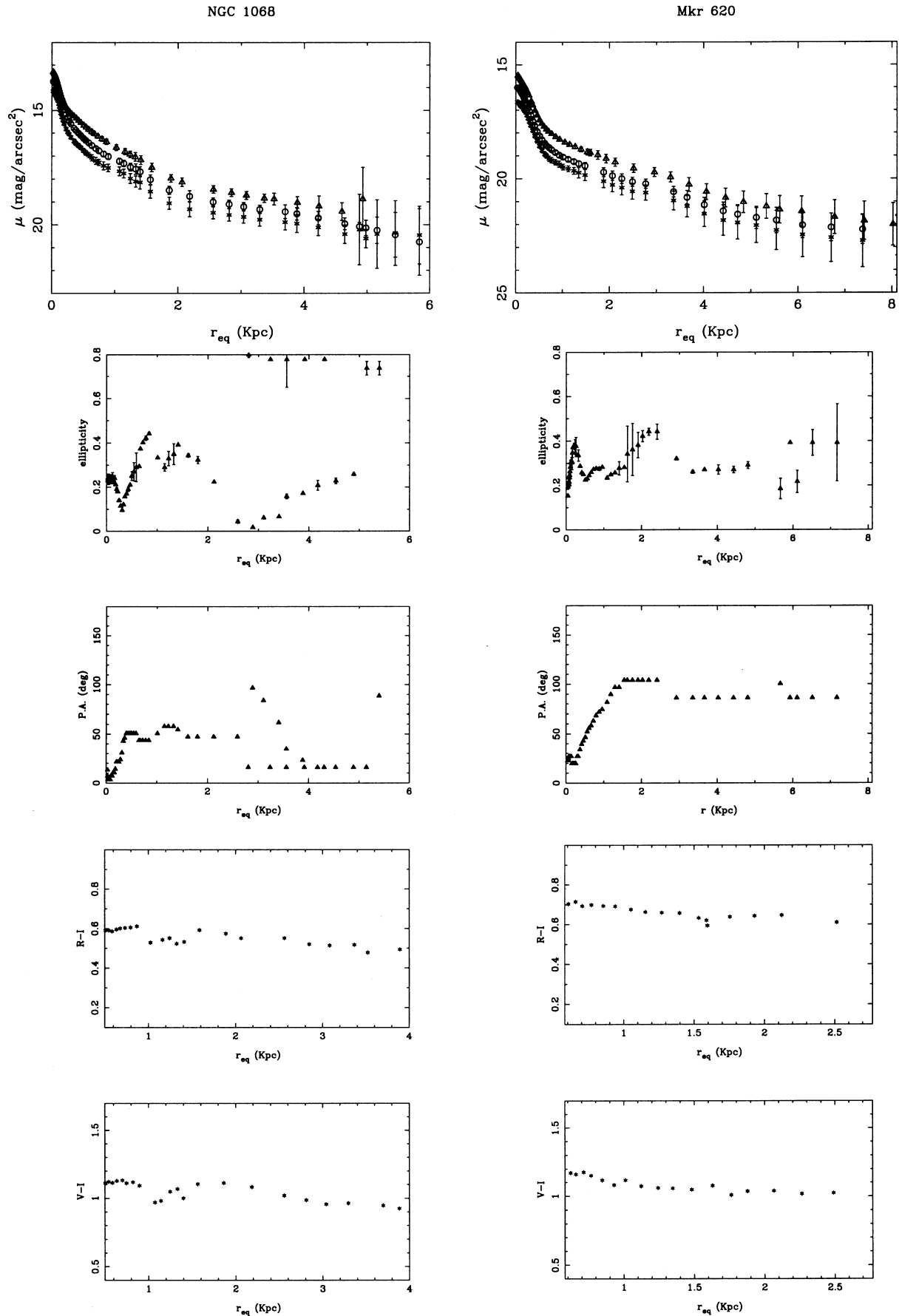


**Figure 12.** Top panel: surface brightness profiles in the V (\*), R (○) and I (△) bands; middle panels: I-band ellipticity and polar angle profiles; bottom panels: R – I and V – I colour profiles.

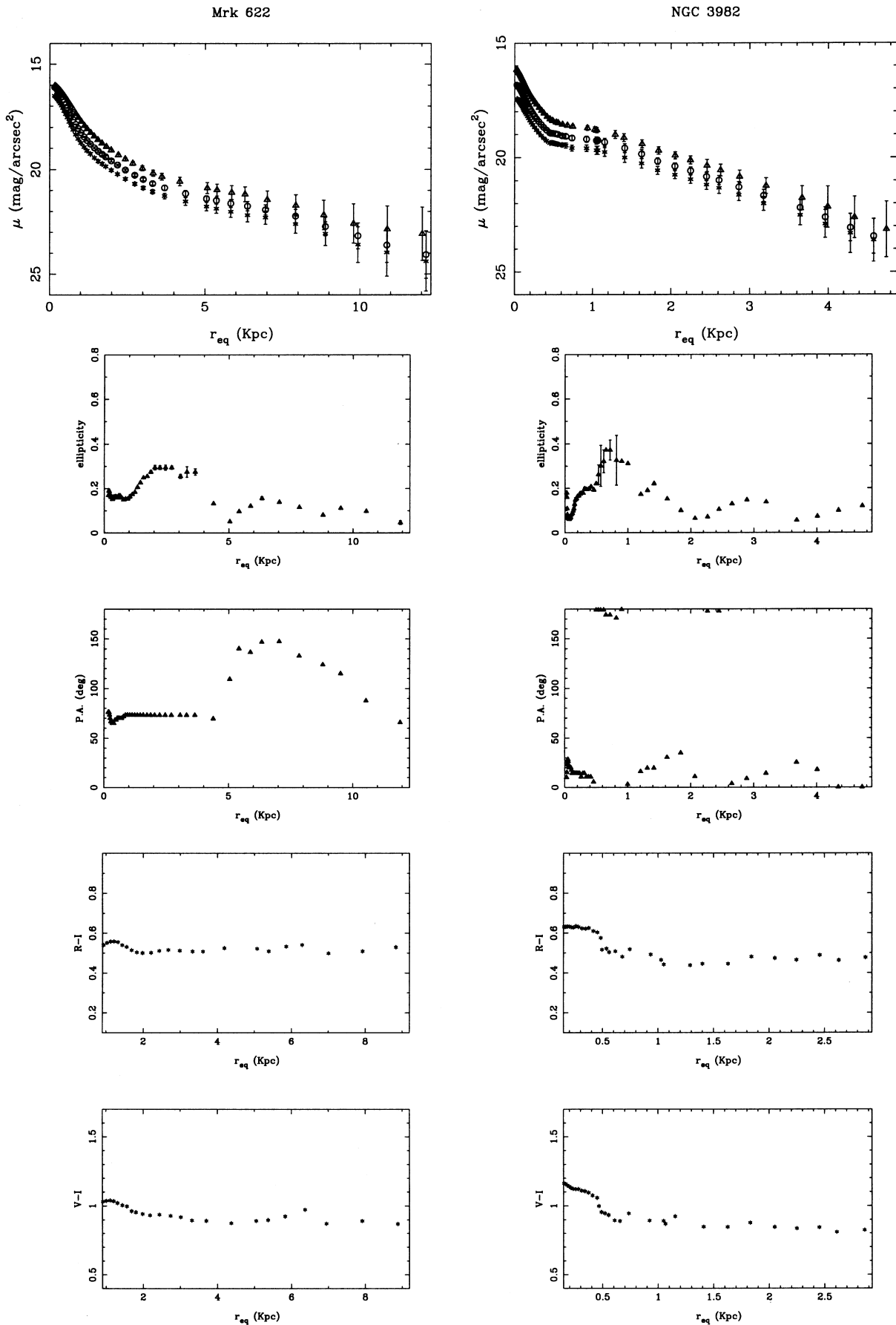


**Figure 13.** Top panel: surface brightness profiles in the V (\*), R (O) and I ( $\Delta$ ) bands; middle panels: I-band ellipticity and polar angle profiles; bottom panels:  $R - I$  and  $V - I$  colour profiles.

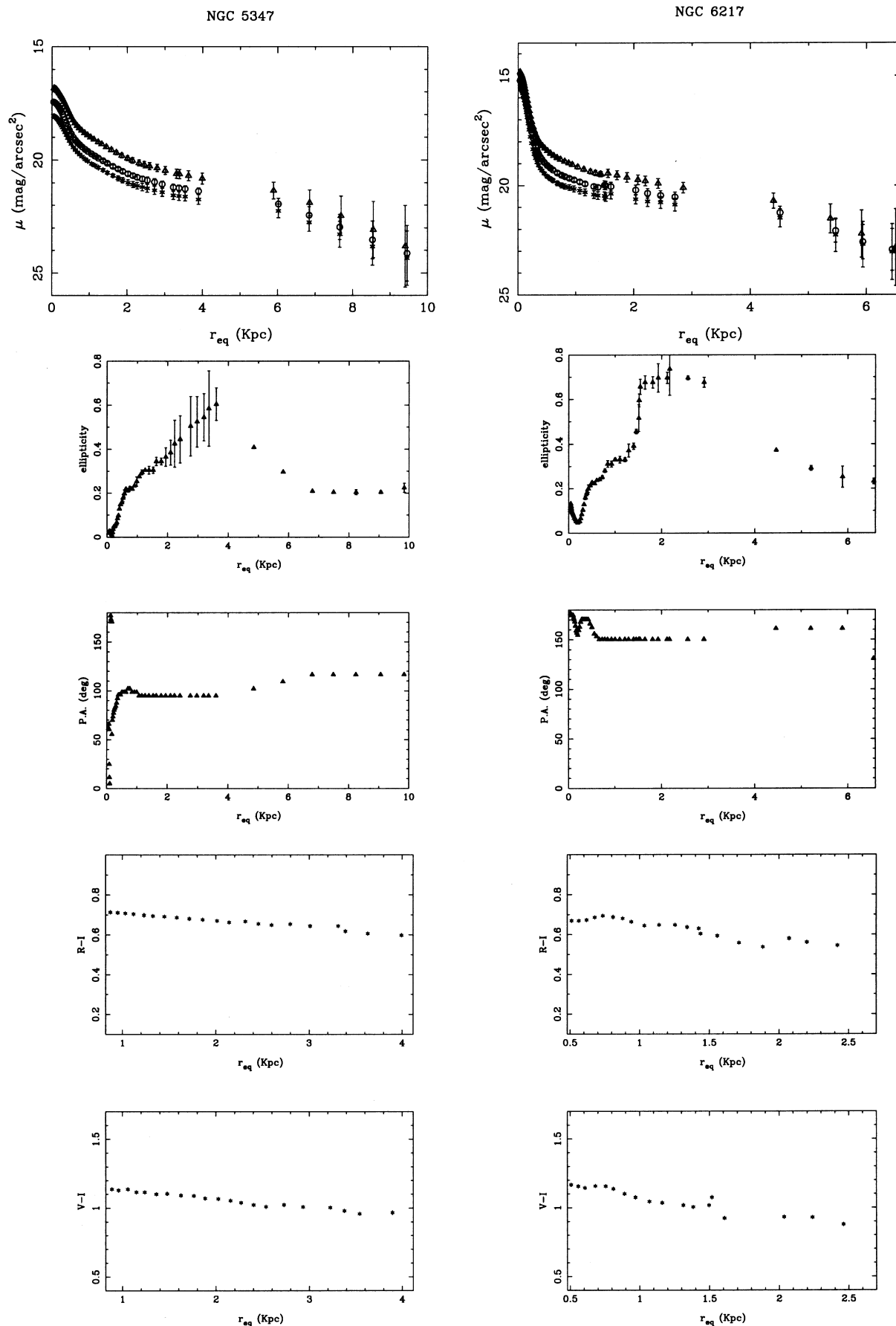


**Figure 14.** Top panel: surface brightness profiles in the  $V$  (\*),  $R$  ( $\circ$ ) and  $I$  ( $\triangle$ ) bands; middle panels:  $I$ -band ellipticity and polar angle profiles; bottom panels:  $R-I$  and  $V-I$  colour profiles.

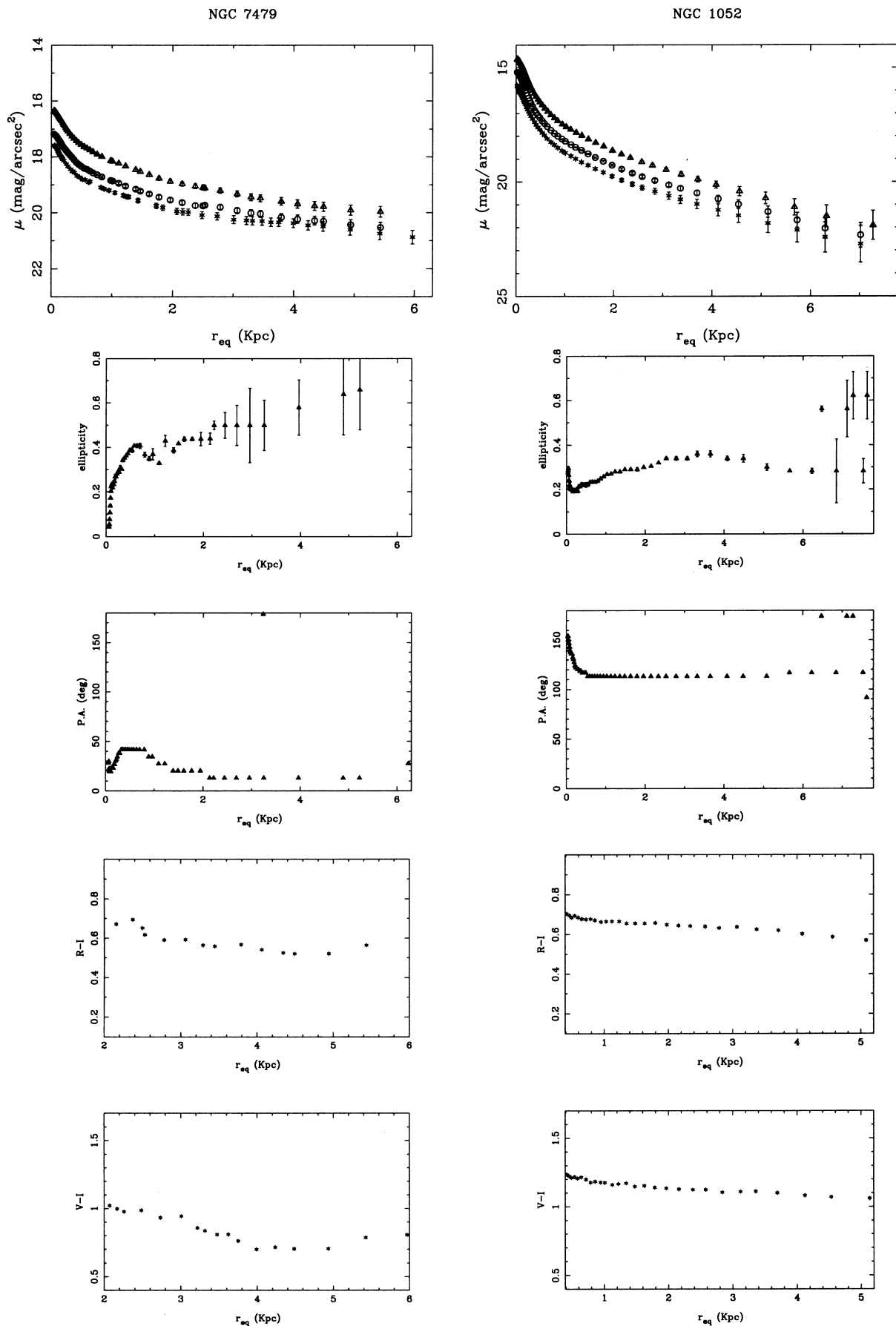


**Figure 15.** Top panel: surface brightness profiles in the V (\*), R (○) and I (△) bands; middle panels: I-band ellipticity and polar angle profiles; bottom panels: R – I and V – I colour profiles.

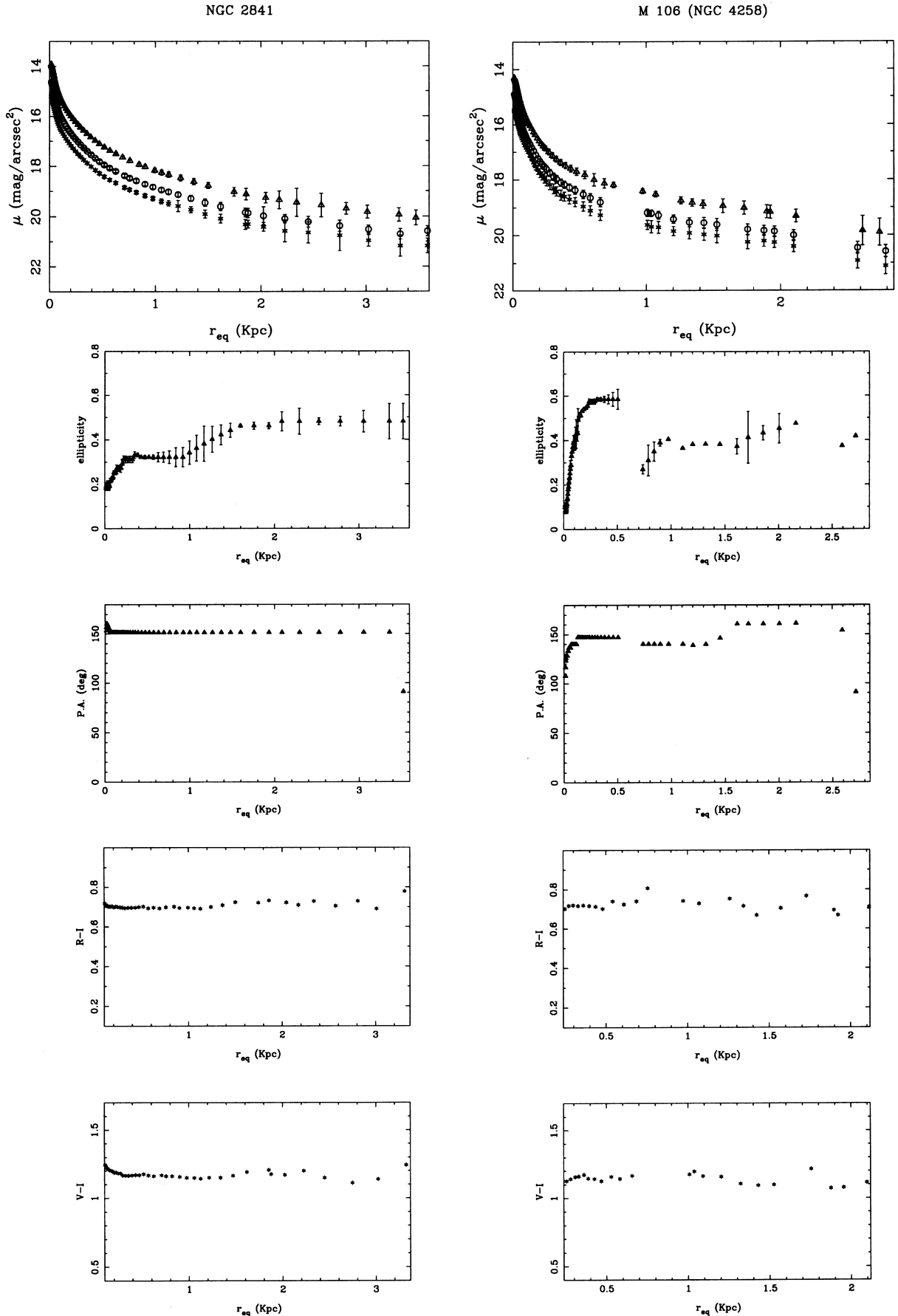


**Figure 16.** Top panel: surface brightness profiles in the V (\*), R (○) and I (△) bands; middle panels: I-band ellipticity and polar angle profiles; bottom panels: R – I and V – I colour profiles.

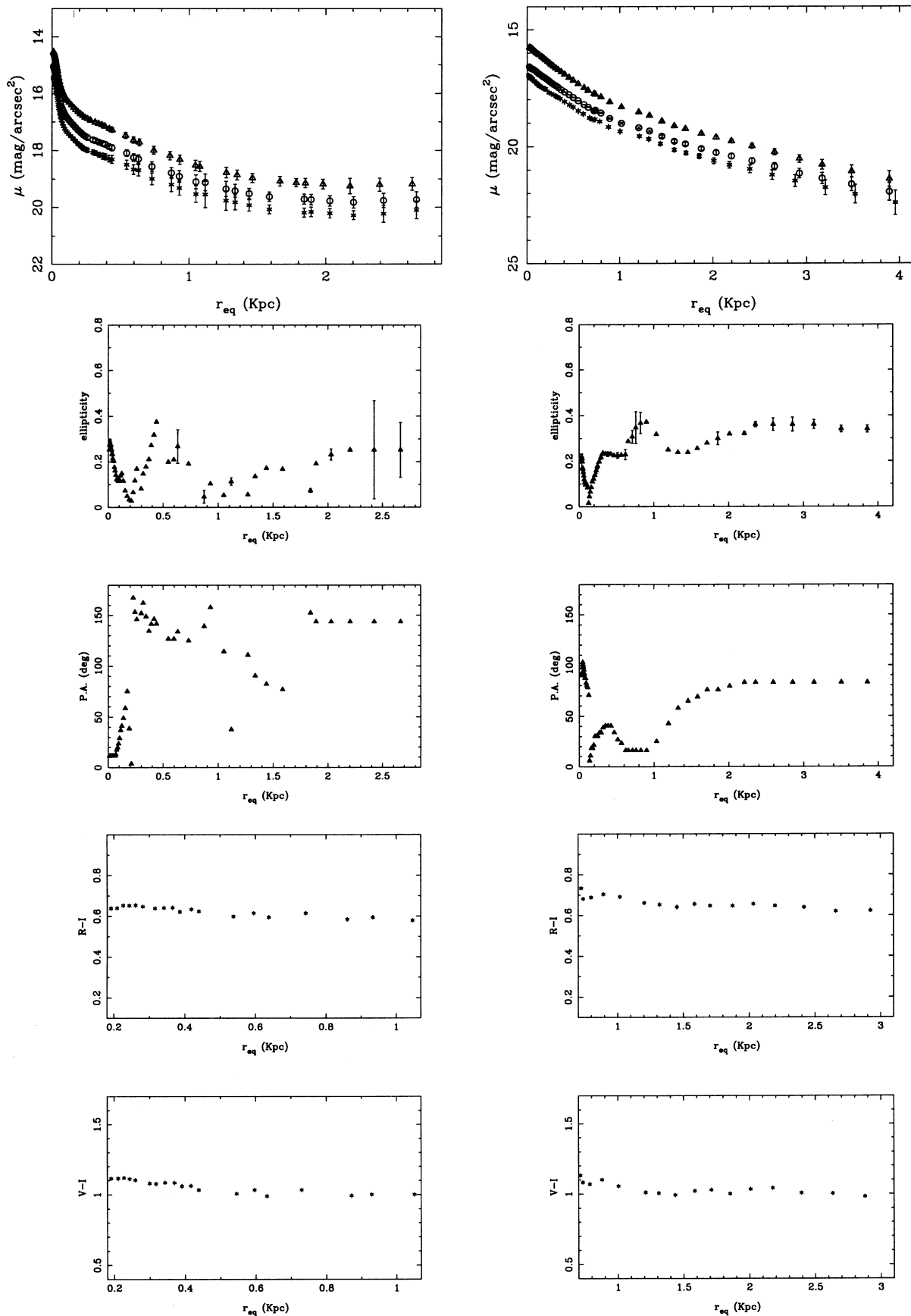


**Figure 17.** Top panel: surface brightness profiles in the V (\*), R (O) and I ( $\Delta$ ) bands; middle panels: *I*-band ellipticity and polar angle profiles; bottom panels: *R* – *I* and *V* – *I* colour profiles.

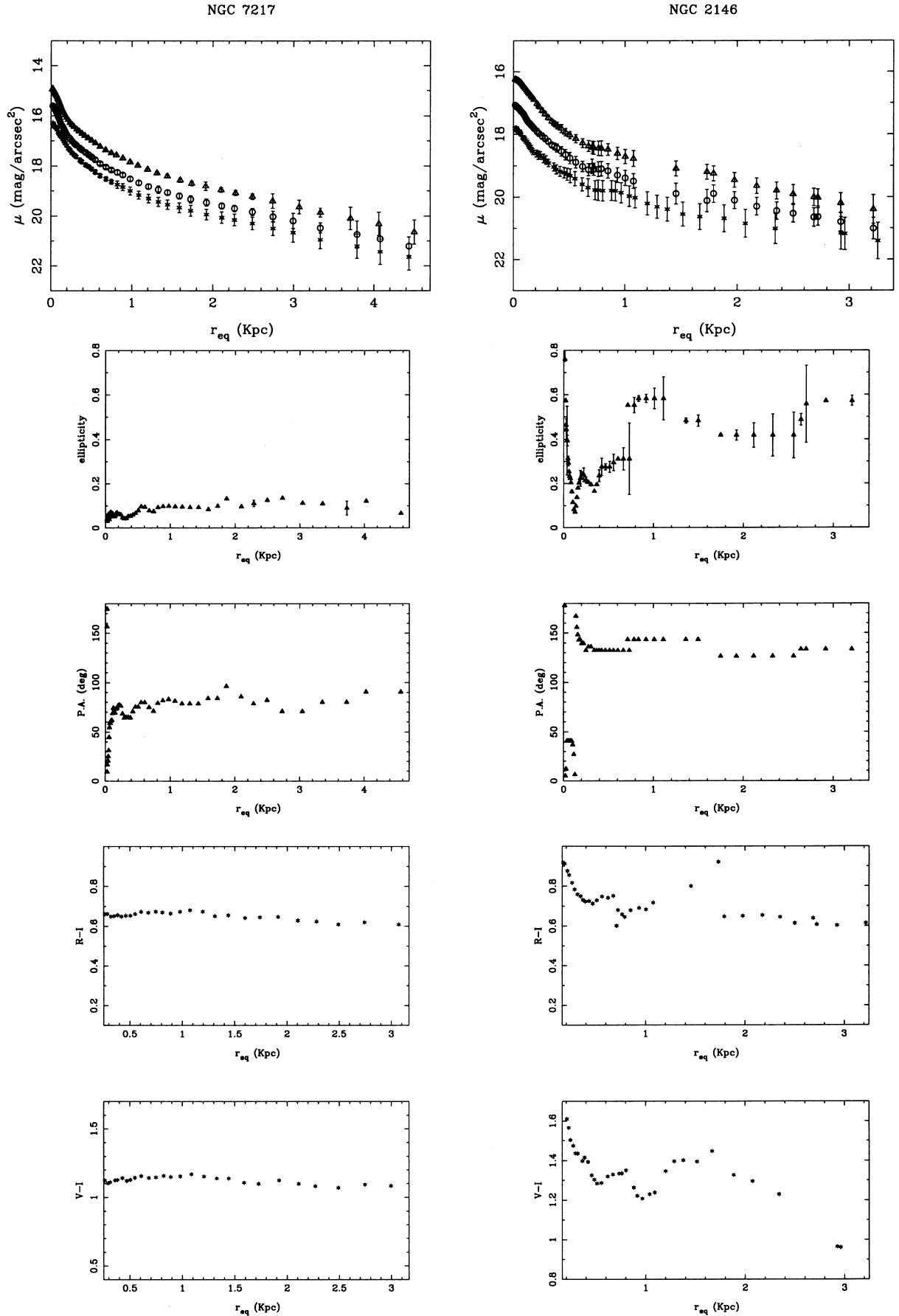


**Figure 18.** Top panel: surface brightness profiles in the V (\*), R (○) and I (Δ) bands; middle panels: I-band ellipticity and polar angle profiles; bottom panels:  $R-I$  and  $V-I$  colour profiles.

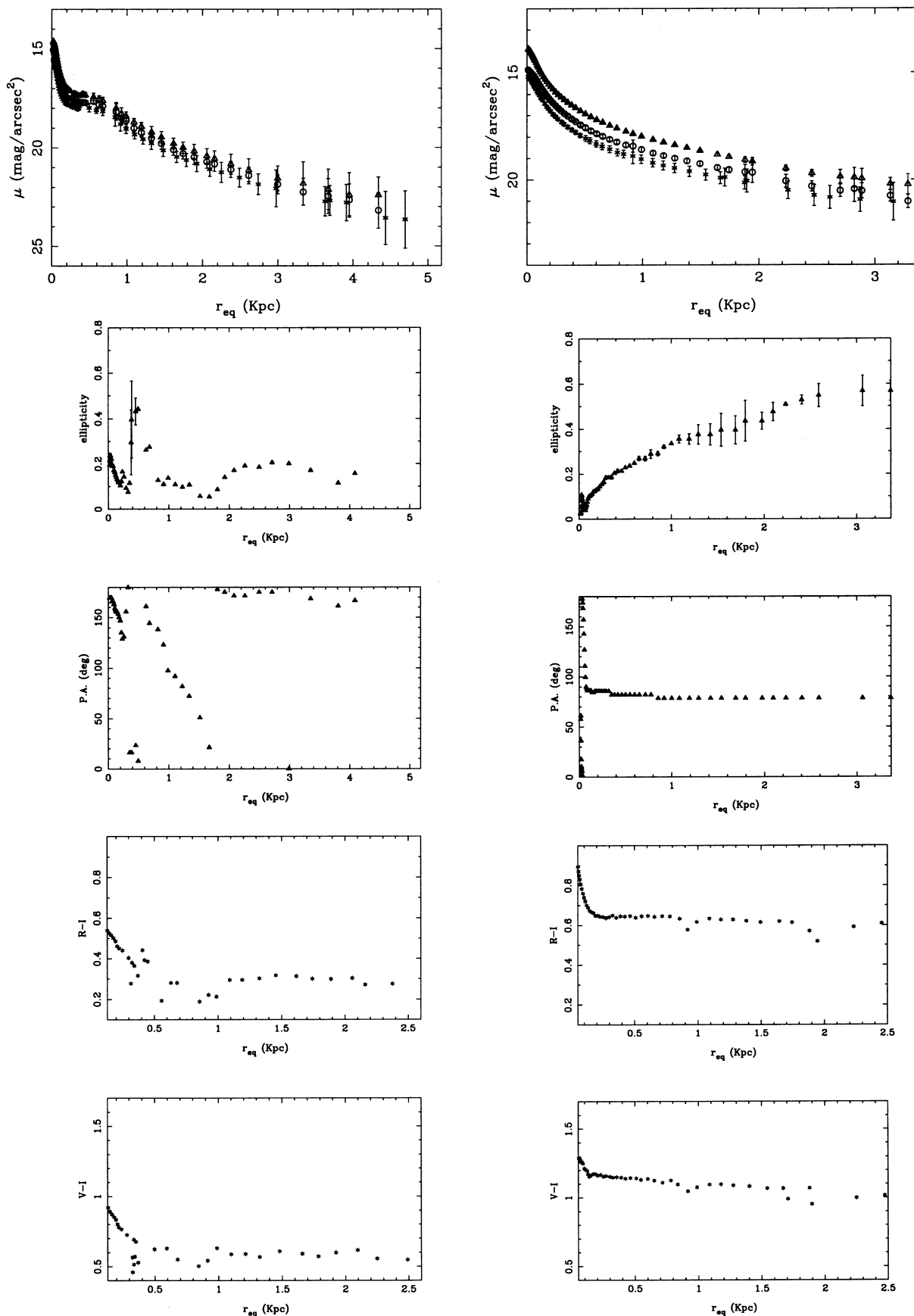


**Figure 19.** Top panel: surface brightness profiles in the  $V^*$  ( $*$ ),  $R$  ( $\circ$ ) and  $I$  ( $\triangle$ ) bands; middle panels:  $I$ -band ellipticity and polar angle profiles; bottom panels:  $R-I$  and  $V-I$  colour profiles.

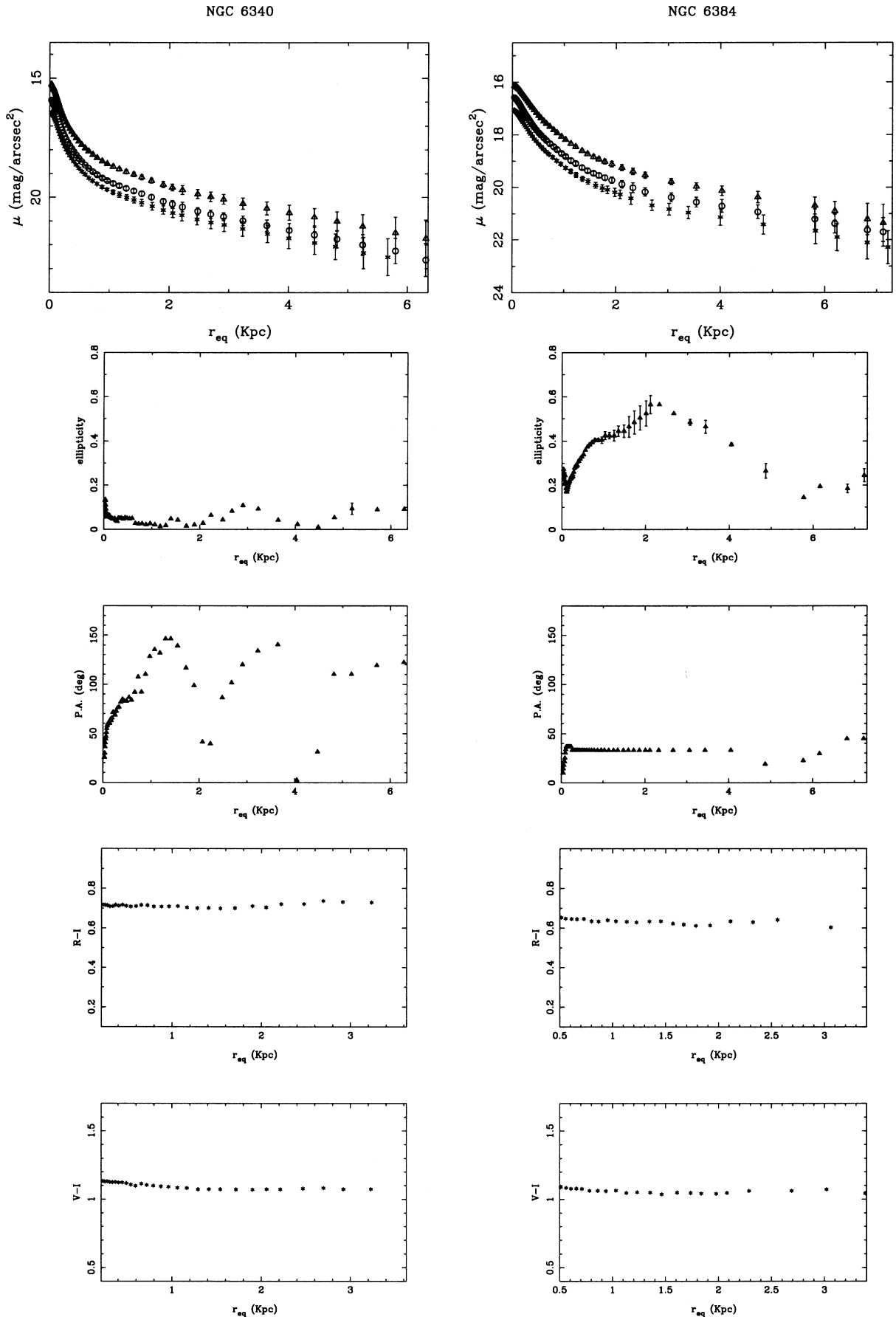


Figure 20. Top panel: surface brightness profiles in the V (\*), R (○) and I (Δ) bands; middle panels: I-band ellipticity and polar angle profiles; bottom panels: R – I and V – I colour profiles.

strong, well-localized, hump-like inner isophotal twist or a jump in the polar angle profile; outer isophotal twists may result from tidal effects (Nieto et al. 1992). In many cases, the criteria coincide with the previous morphological classification given in RC3 (Table 2). However, there are several important features and discrepancies.

(1) NGC 3227. We fail to detect a bar from our ellipticity and polar angle profiles. In our images, a large-scale bar-like shape is seen at  $PA \sim 160^\circ$ ; the  $K_s$  ellipticity profile from Mulchaey et al. (1997), shows a maximum at about 50 arcsec (5 kpc), but cannot trace the full length of the bar.

(2) NGC 4151. While not obvious in our frames, a large-scale bar with  $PA \sim 130^\circ$  is clearly seen in photographic  $U$  and IIIa-J

plates from Simkin (1975). Our ellipticity profile, very close to the  $K_s$  one from Mulchaey et al. (1997), shows a maximum at  $r_{eq} \approx 4.2$  kpc.

(3) NGC 513. A clear hump-like isophotal twist is observed at  $r_{eq} \approx 1.2$  kpc, indicating the possible existence of a bar at  $PA \sim 115^\circ$ ; there is no previous morphological classification. The broad-band images show two weak spiral arms tightly bound to the bulge. These features lead us to classify this galaxy as SABA.

(4) NGC 1068. A maximum in ellipticity is seen at  $r_{eq} \approx 1$  kpc, with  $PA \sim 60^\circ$ . The bar is also clearly seen in the broad-band images, confirming previous results (e.g. Scoville et al. 1988; Thronson et al. 1989; Xanthopoulos 1996). Its classification should therefore be modified from SAb to SABb.

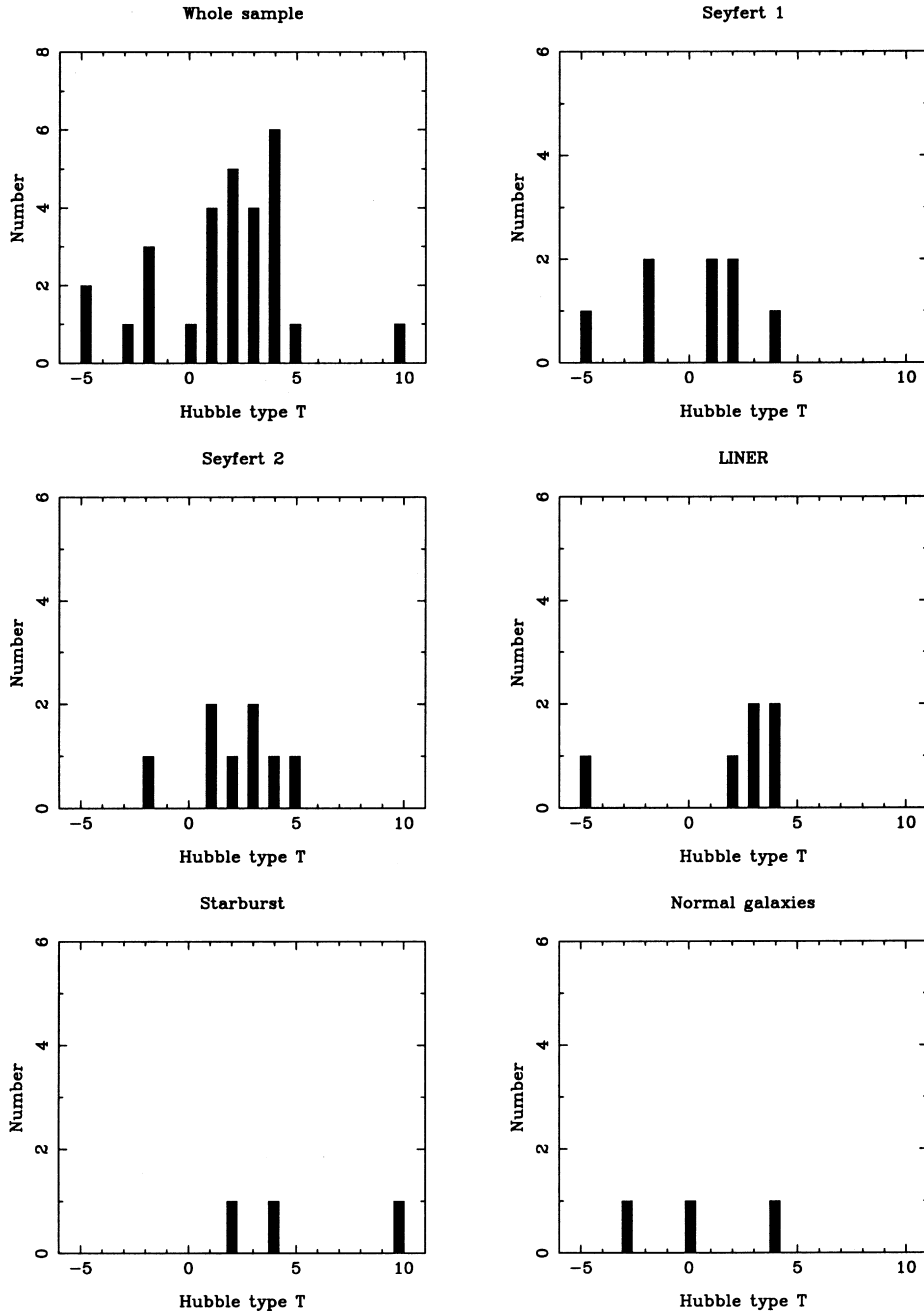


Figure 21. Distribution of morphological Hubble types of the sample galaxies.

(5) Mrk 622. A clear maximum in ellipticity at  $r_{\text{eq}} \approx 2$  kpc is observed; there is no previous accurate morphological classification for this galaxy. MacKenty (1990) classifies this object as S0/a. While the galaxy has a disc, we did not observe any trace of spiral structure. Therefore we classify the galaxy as SB0.

(6) M51. A local maximum in ellipticity is seen at  $r_{\text{eq}} \approx 0.45$  kpc, with PA  $\sim 150^\circ$ . This effect can be due either to a small inner bar or to the presence of the tightly bound spiral arms. We still consider this galaxy as unbarred.

#### 4 DISCUSSION

Fig. 21 shows the distribution of Hubble morphological types ranging from ellipticals ( $T = -5$ ) to irregulars ( $T = -10$ ) according to the nuclear type for the sample galaxies. The reduced size of the sample prevents us from performing a detailed statistical analysis. The greatest frequency corresponds to early-type spirals, from Sa ( $T = 1$ ) to Sbc ( $T = 4$ ). Three out of 15 of the Seyfert nuclei lie in lenticular galaxies of S0 ( $T = -2$ ) and S0a ( $T = 0$ ) type. This ratio is lower than that observed in Xanthopoulos (1996) sample, 44 per cent (12 out of 27), and close to that obtained by MacKenty (1990), 18–27 per cent for a sample of 51 galaxies. On the other hand, a slight tendency for Seyfert 2 nuclei to inhabit galaxies of later morphological type than Seyfert 1 nuclei, can be guessed from our sample data. Khachikian & Weedman (1971) observed certain preference for Seyfert 2 nuclei to lie in spiral galaxies, and in amorphous objects in the case of Seyfert 1 nuclei. Our LINERs appear generally in early spirals, while the starburst galaxies are spirals of type Sab and Sbc.

As stated before, there are controversial clues about the connection between bars and nuclear activity. Table 5 shows the incidence of bars (according to our revised classification) in the different nuclear types of the sample. A high fraction of the objects that present any kind of nuclear activity, about 71 per cent, are barred. This fraction is higher if only Seyfert galaxies are considered, about 87 per cent ( $\sim 71$  per cent of Seyfert 1 galaxies, 100 per cent of Seyfert 2). These values are higher than those obtained by MacKenty (1990) (about 30 per cent in spiral galaxies) and Xanthopoulos (1996) (42 per cent in Seyfert 1 and 60 per cent in Seyfert 2), and similar to the fraction obtained by Simkin, Su & Schwartz (1980) (about 70 per cent). If we adopt a mean value of 59 per cent of barred objects for galaxies of any nuclear kind (Simkin et al. 1980), our result can reinforce the clues of connection between bars and nuclear activity. Nevertheless, near-infrared  $K_s$  band observations from Mulchaey et al. (1997) of a sample of 33 Seyfert galaxies and the same number of normal galaxies reveal that the incidence of bars in the sample Seyfert and normal galaxies is roughly the same, about 70 per cent; many normal galaxies formerly classified as unbarred show bars in the near-infrared. On the other hand, a significant fraction of Seyfert galaxies do not present evidence of bars even in the

near-infrared. Mulchaey & Regan (1997) suggest that maybe kiloparsec-scale bars are not a universal fuelling mechanism in Seyfert galaxies; alternatively, a possible explanation for the lack of bars in some Seyfert galaxies is that the bars were recently destroyed, possibly by the formation of the central black hole.

#### ACKNOWLEDGMENTS

We are grateful to Emily Xanthopoulos for her critical analysis that largely contributed towards improving the paper.

The JKT is operated on the island of La Palma by the Isaac Newton Group in the Spanish Observatorio del Roque de los Muchachos of the Instituto de Astrofísica de Canarias. We thank CAT for awarding observing time.

#### REFERENCES

- Alvarez Alvarez M., 1997, Master's thesis, Univ. Autónoma de Madrid  
 Argyle R. W., Mayer C. J., Pike C. D., Jordan P. R., 1998 (February), A User Guide to the JKT CCD Camera,  
 Arsenault R., 1989, *A&A*, 217, 66  
 Burstein D., Heiles C., 1984, *ApJS*, 54, 33  
 Davies L. E., Cawson M., Davies R. L., Illingworth G., 1985, *AJ*, 90, 169  
 De Robertis M. M., Hayhoe K., Yee H. K. C., 1998, *ApJS*, 115, 163  
 de Vaucouleurs G., de Vaucouleurs A., Corwin H. G., Jr, 1976, Second Reference Catalog of Bright Galaxies, Univ. Texas Monograph. Univ. Texas Press, Austin (RC2)  
 de Vaucouleurs G., de Vaucouleurs A., Corwin H. G. Jr., Buta R., Paturel G., Fouqué P., 1991, Third Reference Catalog of Bright Galaxies. Springer, New York (RC3)  
 Ford H. C., Crane P. C., Jacoby G. H., Lawrie D. G., van der Hulst J. M., 1985, *ApJ*, 293, 132  
 Fosbury R. A. E., Mebold U., Goss W. M., Dopita M. A., 1978, *MNRAS*, 183, 549  
 Granato G. L., Zitelli V., Bonoli F., Danese L., Bonoli C., Delpino F., 1993, *ApJS*, 89, 35  
 Heckman T. M., 1980a, *A&A*, 87, 142  
 Heckman T. M., 1980b, *A&A*, 87, 152  
 Ho L. C., Filippenko A. V., Sargent W. L. W., 1995, *ApJS*, 98, 477  
 Hunt L. K., Malkan M. A., Salvati M., Mandolesi N., Palazzi E., Wade R., 1997, *ApJS*, 108, 229  
 Khachikian E. Y., Weedman D. W., 1971, *Afz*, 7, 389  
 Kodaira K., Okamura S., Ichikawa S., 1990, Photometric Atlas of Northern Bright Galaxies. Univ. Tokyo Press  
 Kotilainen J. K., Ward M. J., 1994, *MNRAS*, 266, 953  
 Landolt A. U., 1983, *AJ*, 88, 439  
 MacKenty J. W., 1990, *ApJS*, 72, 231  
 Márquez I., Moles M., 1994, *AJ*, 108, 90  
 Massey P., Strobel K., Barnes J. V., Anderson E., 1988, *ApJ*, 328, 315  
 Mulchaey J. S., Regan M. W., 1997, *ApJ*, 482, L135  
 Mulchaey J. S., Regan M. W., Kundu A., 1997, *ApJS*, 110, 299  
 Nieto J. L., Bender R., Poulain P., Surma P., 1992, *A&A*, 257, 97  
 Norman C., Scoville N., 1988, *ApJ*, 332, 124  
 Pedlar A., Kukula M. J., Longley D. P. T., Muxlow T. W. B., Axon D. J., Baum S., O'Dea C., Unger S. W., 1993, *MNRAS*, 263, 471  
 Penston M. V. et al., 1981, *MNRAS*, 196, 857  
 Perry J. J., 1992, in Filippenko A. V., ed., ASP Conf. Ser. Vol. 31, Relationships between Active Galactic Nuclei and starburst Galaxies. Astron Soc. Pac., San Francisco, p. 169  
 Pogge R. W., 1989a, *ApJ*, 345, 730  
 Pogge R. W., 1989b, *ApJS*, 71, 433  
 Rees M. J., 1984, *ARA&A*, 22, 471  
 Sánchez-Portal M., 1996, PhD thesis, Univ. Autónoma de Madrid  
 Schweizer F., 1983, in Athanassoula E., ed., Internal Kinematics and Dynamics of Galaxies. Reidel, Dordrecht, p. 319

**Table 5.** Bar incidence versus nuclear type.

Nuclear type	Barred		Unbarred	Elliptical
	SB type	SAB type		
Sy 1	1	4	1	1
Sy 2	5	3	0	0
LINER	0	2	3	1
Starburst	1	1	1	0
Total	17		5	2

- Scoville N. Z., Matthews K., Carico D. P., Sanders D. B. 1988, *ApJ*, 327, L61
- Seaton M. J., 1975, *MNRAS*, 170, 475
- Simkin S. M., 1975, *ApJ*, 200, 567
- Simkin S. M., Su H. J., Schwarz M. P., 1980, *ApJ*, 237, 404
- Stone R. P. S., 1977, *ApJ*, 218, 767
- Terlevich R. J., 1992 in Filippenko, A. V. ed., *ASP Conf. Ser. Vol. 31, Relationships between Active Galactic Nuclei and Starburst Galaxies.* Astron. Soc. Pac., San Francisco, p. 133
- Terlevich R. J., Sánchez-Portal M., Díaz A. I., Terlevich E., 1991, *MNRAS*, 249, 36
- Thronson H. A., Jr et al., 1989, *ApJ*, 343, 158
- Ulvestad J., Wilson A. S., 1984, *ApJ*, 285, 439
- Ulvestad J., Wilson A. S., Sramek R. A., 1981, *ApJ*, 247, 419
- Varela A. M., 1992, PhD thesis, Instituto de Astrofísica de Canarias,
- Véron-Cetty M. P., Véron P., 1985, *A Catalogue of Quasars and Active Nuclei.* ESO Scientific Report No. 4,
- Wrobel J. M., Heeschen D. S., 1988, *ApJ*, 335, 677
- Xanthopoulos E., 1996, *MNRAS*, 280, 6
- Yee H. K., 1983, *ApJ*, 272, 473

This paper has been typeset from a  $\text{\TeX/L\AA\TeX}$  file prepared by the author.